

UC Berkeley

UC Berkeley Electronic Theses and Dissertations

Title

Ultrafast Magnetization Dynamics in the Presence of Strong Spin-Orbit Coupling

Permalink

<https://escholarship.org/uc/item/5zd9d92n>

Author

Kantner, Colleen

Publication Date

2010

Peer reviewed|Thesis/dissertation

Ultrafast Magnetization Dynamics in the Presence of Strong Spin-Orbit Coupling

by

Colleen Leanna Stallard Kantner

A dissertation submitted in partial satisfaction of the

requirements for the degree of

Doctor of Philosophy

in

Physics

in the

Graduate Division

of the

University of California, Berkeley

Committee in charge:

Professor Joseph Orenstein, Co-Chair

Professor R. Ramesh, Co-Chair

Professor Joel Moore

Professor Junqiao Wu

Spring 2010

Ultrafast Magnetization Dynamics in the Presence of Strong Spin-Orbit Coupling

Copyright 2010

by

Colleen Leanna Stallard Kantner

Abstract

Ultrafast Magnetization Dynamics in the Presence of Strong Spin-Orbit Coupling

by

Colleen Leanna Stallard Kantner

Doctor of Philosophy in Physics

University of California, Berkeley

Professor Joseph Orenstein, Co-Chair

Professor R. Ramesh, Co-Chair

The time-resolved magneto-optical Kerr effect is used to study magnetization dynamics in thin films of SrRuO_3 . This thesis focuses on two topics in particular: the influence of epitaxial strain on magnetization dynamics and magnetic orientation, and the origin of the dramatic slowing down of the demagnetization time near the Curie temperature.

Magnetization dynamics in SrRuO_3 are initiated by a temperature dependent rotation of the magnetocrystalline anisotropy field direction upon thermal excitation by the laser. The resulting dynamics depend on the orientation of the anisotropy field in the sample. We observe a change in the orientation as a function of epitaxially strain by looking at SrRuO_3 grown on various substrates with (001) orientation and distinct in-plane lattice parameters. We find that in SrRuO_3 films under compressive strain, the anisotropy field moves in a plane perpendicular to the film surface. Beyond a certain degree of tensile strain, the anisotropy field moves in the plane parallel to the surface of the film. Support of this result from theoretical calculations and XRD measurements is discussed and attempts to strain tune films with a piezoelectric substrate are described.

Near the Curie temperature, the demagnetization time in $\text{SrRuO}_3/\text{SrTiO}_3(111)$ is found to increase by more than a factor of ten. Here, we study this effect in detail and derive an equation for the demagnetization time in terms of the spin flip time, starting from detailed balance and borrowing from a recent spin-based model for demagnetization[57, 58]. The demagnetization time is found to be proportional to the spin flip time and inversely proportional to the reduced temperature near T_c , allowing us to measure the spin flip time. We also relate the spin flip time and the damping parameter to the Curie temperature and find that the previously speculated upon relationship between the damping parameter in SrRuO_3 and the anomalous Hall effect is strengthened.

To my parents, Jeff and Susan
and my siblings, Kevin and Maureen

Contents

List of Figures	iv
1 Introduction	1
1.0.1 The Spin-Orbit Interaction	2
2 SrRuO₃ Thin Films	4
2.1 Structural Properties of SrRuO ₃	4
2.2 Film Growth	6
2.2.1 Samples for demagnetization experiments	6
2.2.2 Samples for strain experiments	6
2.3 Electronic Properties	7
2.3.1 Non-Fermi Liquid Behavior in SRO	7
2.3.2 Anomalous Hall Effect	8
2.4 Magnetic Properties	9
2.4.1 Itinerant Ferromagnetism	9
2.4.2 The Stoner Model	9
2.4.3 Mean Field Theory	11
2.5 Magnetic Anisotropy	12
2.5.1 Magnetocrystalline Anisotropy	12
2.5.2 Shape Anisotropy	13
2.5.3 Inverse Magnetostriction	13
2.5.4 Anisotropy in SRO	14
2.6 Strain Effects	15
3 Ultrafast Magnetization Dynamics	18
3.1 Theory of Magnetization Dynamics	18
3.1.1 The Landau-Lifshitz-Gilbert Equation	18
3.1.2 Determining Magnetization Dynamics from the Free Energy Potential	20
3.2 Damping	22
3.2.1 Intrinsic Damping	22
3.2.2 Extrinsic damping	24
3.3 Theory of Ultrafast Demagnetization	24
3.3.1 The Elliott-Yafet Mechanism	25
3.3.2 Three Temperature Model	25

3.3.3	Koopmans' Model	26
4	Experimental Technique	28
4.1	Initiating Demagnetization and Magnetic Precession in SrRuO ₃	28
4.2	The Magneto-Optical Kerr Effect	29
4.2.1	Phenomenological Description	29
4.2.2	Quantum Mechanical Origin	32
4.3	Time-Resolved MOKE Measurements	32
4.3.1	Optical Set-up	34
4.3.2	Detection and Data Acquisition	36
4.3.3	Derivative Measurements	37
4.3.4	Optical Bleaching Effects	38
4.4	Cryostats	38
5	Strain Effects on Anisotropy Orientation and Magnetization Dynamics in SRO	39
5.0.1	Previous Work: Ferromagnetic Resonance in SRO	39
5.1	Strained Samples	41
5.2	Strain Effects on Magnetization Dynamics	42
5.3	Analysis: Anisotropy Reorientation as a Function of Strain	44
5.3.1	Fourier Analysis	45
5.3.2	Theoretical Support	46
5.3.3	Support from X-ray Diffraction Experiments	47
5.4	Intermediate Behavior	48
5.5	Switching Between Orientations	48
5.5.1	Experimental Challenges	50
6	Magnetization Dynamics Near the Curie Temperature	53
6.1	Critical Slowing Down	53
6.2	Results from Time-Resolved MOKE measurements on SRO/STO(111)	54
6.3	Deriving the Demagnetization time from the Spin-flip time near T _c	58
6.4	Relating the spin-flip time to the damping parameter	61
6.5	Demagnetization and damping	62
7	Summary	64
	Bibliography	65

List of Figures

2.1	Idealized cubic structure of SRO.	5
2.2	Orthorhombic structure of SRO, showing oxygen octahedra rotations. From [108].	5
2.3	Possible orthorhombic orientations of SRO on substrates with (001) orientation. On the left is the (110) orientation, and on the right is the (001) orientation. From [46]	7
2.4	Left: Diagram of band shifting in the Stoner Model. \mathcal{E} is total energy: magnetic + kinetic. Right: Calculated density of states for SRO. [3]	10
2.5	Left: Graphical method to determine magnetization from mean field theory. Above T_c there is only one solution, $M = 0$. Below T_c three solutions exist: $M = 0, \pm M_0$ [37]	12
2.6	In-plane (red), out-of-plane (blue), and total magnetization (black) as a function of temperature. The angle of the easy axis relative to the sample normal is shown in the inset. Figure from [51].	15
2.7	Epitaxial growth of SRO on STO. The in-plane lattice parameter is compressed. 16	
2.8	Rotation of the RuO_6 octahedra as a function of strain in SRO. The top plot shows the rotation for (001) SRO and the bottom plot shows the rotation for (110) SRO. The relevant calculations in the top plot are labeled ‘FM’ for ferromagnetic. From [51].	17
3.1	Schematic of spherical coordinates.	20
3.2	On the left, a schematic representation of the three temperature model. On the right, an increase in spin temperature leads to a reduction of the total magnetization. Figure from [23]	26
4.1	Schematic of thermally induced magnetic precession.	29
4.2	Schematic of the energy levels in a ferromagnet, showing the electric dipolar optical transitions for left and right circular light. On the right are the corresponding absorption spectra versus photon energy. Figure from [14] . .	33
4.3	Diagram of time-resolved pump-probe setup	34
4.4	Time-Resolved magneto-optical Kerr effect	36
5.1	Change in Kerr rotation on 200nm SRO/STO(001) as a function of time delay following photoexcitation, in the temperature range $5 < T < 80\text{K}$	40
5.2	Fourier transform of TRMOKE signal in an applied magnetic field of up to 6T 40	

5.3	Lattice parameters of strained SRO films. The in-plane substrate lattice parameter is plotted on the x-axis and the out-of-plane lattice parameter of the film is plotted on the y-axis.	41
5.4	TRMOKE signal at 5K after photoexcitation at time $t = 0$ for 10nm SRO films on STO, DSO, DSO*, DSO**, and GSO substrates	43
5.5	Colored arrows indicate the relevant strained samples for the TRMOKE data in the above figure. Compare to figure 5.3	43
5.6	Possible orientations of SRO films on (001) oriented substrates. The blue arrows indicate the corresponding motion of the anisotropy field in each case.	44
5.7	Real and imaginary parts of the Fourier transform for SRO/STO (top) and SRO/DSO* (bottom). The signals appear to be out of phase with each other.	46
5.8	Energy of lattice orientation calculated as a function of epitaxial strain for CaTiO ₃ . From [27].	47
5.9	Difference in the phase of the Fourier transform for SRO grown on various substrates with SRO/STO. The black lines indicate phase shifts of 45 and 90°	49
5.10	Phase difference with SRO/STO at the frequency peak for SRO films from above plot. The near linear dependence suggests a correlation between these two properties.	49
5.11	Strain induced in a film by bending the substrate.	51
6.1	Derivative of the change in Kerr rotation as a function of time delay following pulsed photoexcitation, for $5 < T < 85$ K	54
6.2	Change in Kerr rotation as a function of time delay following pulsed photoexcitation, for $120 < T < 165$ K	55
6.3	Comparing amplitudes of the short time feature and the ferromagnetic resonance oscillations in figure 6.1 as function of temperature.	56
6.4	Temperature dependence of the (a) amplitude of oscillations, (b) FMR frequency, and, (c) damping parameter for SRO/STO(111)	57
6.5	Temperature dependence of FMR frequency and damping parameter for SRO/STO(001). Adapted from [66]	57
6.6	The demagnetization time as a function of temperature near T_c	58
6.7	Log-log plot of the demagnetization time as a function of reduced temperature near T_c	60
6.8	Spin flip time at high temperature	61

Acknowledgments

This work would not have been possible without the contributions of a number of people. I would like to acknowledge:

my advisors,

Joe, the rare experimentalist also capable of theory work, for his vast knowledge of physics, his well-considered perspective, and his sense of humor

Ramesh, for his inspiring passion and energy

my labmates,

Jake, for helpful conversations, and always being willing to provide a distraction from working

Luyi, for her determination and example

Jamie, for bringing new enthusiasm into the group

the numerous people who grew/characterized/processed samples for me, especially Wolter, Lane, and John, who considerably expanded my knowledge of materials science

Rene from the machine shop, the vacuum specialists at the ALS, and all the tech support staff who always found a way to squeeze my projects into their busy schedules

the administrative support staff in physics and EECS, particularly Anne Takizawa, for making my life easier

my friends,

Bonnie and DA, for being my home away from home

Andre, Jeff, Harish, who made the early years of grad school such a pleasure, before moving on to bigger and better things

Michael, for encouraging me to study physics as an undergrad, and keeping me sane through all our shared classes and labs

my family,

my parents, for their unwavering support

Kevin and Maureen, for always keeping me humble, mostly via mockery

and Matt, for his patience and support, inside the lab and out

Chapter 1

Introduction

It is important to ask “why” before commencing any scientific inquiry - and useful to remind yourself of this reason periodically, as it is easy to get sidetracked or discouraged. In the case of this thesis, the motivation comes from the increased use of magnetism in technology and the desire to better control that magnetism, as well as the wonder of more fully understanding how magnetism works.

There can be no doubt of the increasing role magnetism plays in technology and today’s society. The ubiquity of ipods, based on giant magneto-resistance (GMR)[5, 11, 86], is just one indicator. Magnetism is also either used or being explored for usage in speakers, cell phones, data storage, sensors, and logic. And who knows what sector might be revolutionized next by a scientific breakthrough?

Two areas of particular research interest with regard to magnetism are the speed with which a magnetic state can be changed and the ability to control that magnetic state with an electric field.

The speed at which magnetic data-storage elements can be manipulated is ultimately dependent on elementary spin-scattering processes and how they influence the demagnetization of the material used in femtosecond laser-writing schemes. But despite its technological relevance, demagnetization is still not well understood on a microscopic level.

It is not surprising that there is significant interest in applying electric fields to change magnetization. Currently, in order to change the orientation of a magnetic field it is necessary to apply another magnetic field, which is an energetically inefficient process. Applying an electric field to change a magnetization is potentially more energy efficient and easier to integrate into commonly used electronic devices. One way this could be done is through a multiferroic material where electric and magnetic ordering may be directly coupled[104]. Another potential method is to grow a material whose magnetic orientation is dependent on strain on a piezoelectric material. A necessary first step in this latter case is demonstrating that the magnetic orientation changes with strain.

In searching for a material to satisfy both components of our queries we come across SrRuO₃. SrRuO₃ is remarkable for a number of reasons, including its non-Fermi liquid behavior[52] and potential link to the anomalous Hall effect[66]. Most relevantly for us, SrRuO₃ is a material with very strong spin orbit coupling. The spin-orbit interaction provides a mechanism for spin-flip scattering and is responsible for strong magneto-elastic

coupling.

In this thesis, strain induced reorientation and demagnetization are studied in SrRuO₃ via the time resolved magneto-optical Kerr effect.

Previous work has demonstrated that magnetization dynamics associated with ferromagnetic resonance can be measured in SrRuO₃ by the time resolved magneto-optical Kerr effect[66]. Here, we study the effect of strain on those dynamics and the underlying magnetic orientation. This is particularly useful for films grown on paramagnetic substrates which cannot be measured by traditional diagnostics such as SQUID.

A wide dynamic range in demagnetization time in SrRuO₃ near the Curie temperature has been shown previously[80]. Here, we examine this behavior closely and attempt to derive an equation of the demagnetization time near T_c .

This thesis is organized as follows:

Chapter 2 outlines the basic structural, electronic, and magnetic properties of SrRuO₃. Of particular interest are the rotations of the RuO₆ octahedra, the strong electron-electron correlations, and the unusually large magnetocrystalline anisotropy field in SRO. The growth of SRO films for both strain and demagnetization experiments is also described. Toward the end of the chapter, strain effects on structure will be discussed and implications for magnetic properties of SRO will be motivated.

In Chapter 3, theoretical models of magnetization dynamics and demagnetization are outlined. These include the Landau-Lifshitz-Gilbert equation describing collective precessional motion, and the phenomenological three temperature model and Koopmans' model describing demagnetization. Sources of damping, particularly those related to spin-orbit coupling, are also discussed.

Chapter 4 describes how magnetization dynamics can be studied by ultrafast optical experiments. An overview of the magneto-optical Kerr effect is given, and the experimental setup is detailed.

In Chapter 5 the results of magnet-optic measurements on strained SrRuO₃ films are presented and analyzed. The magnetocrystalline anisotropy field direction is found to depend on the epitaxial strain from a substrate. Efforts to strain SrRuO₃ by applying an electric field to a piezoelectric substrates encounter a number of experimental challenges, however, which are described.

Chapter 6 presents the wide dynamic range of demagnetization near the Curie temperature. A relationship between the demagnetization time and the spin-flip time is derived, and the relationship between these parameters and the damping parameter is discussed. The demagnetization time is found to be inversely proportional to the reduced temperature.

1.0.1 The Spin-Orbit Interaction

Since spin-orbit coupling plays such a crucial role in the motivation for these experiments, it makes sense to discuss it immediately. The spin-orbit interaction is the result of the relativistic motion of electrons in the periodic electric potential field of atomic nuclei in the lattice. The electrons see the stationary field of the lattice as a magnetic field.

The Hamiltonian for spin orbit interaction can be written in terms of the electron spin, S , and the angular momentum, L , of the perceived magnetic field of the lattice[36]:

$$H_{SO} = \frac{Ze^2}{2m^2c^2r^3} \mathbf{L} \cdot \mathbf{S} \quad (1.1)$$

where Z is the atomic number of a nucleus, m and e the mass and charge of an electron, respectively, and c is the speed of light.

There are a number of important consequences to this interaction.

The spin-orbit interaction:

1) causes a preferential alignment of spins in a ferromagnet. The interaction determines the magnitude and direction of the magnetocrystalline anisotropy field, and as a result sets the time scale for spin dynamics. (See sections 2.5.1 and 3.1.2)

2) is a necessary component of the Elliot-Yafet mechanism which is responsible for spin flip while scattering, leading to demagnetization. (See section 3.3.1)

3) makes optical measurements of magnetization dynamics possible via the magneto-optical Kerr effect. (See section 4.2.2)

SRO has exceptionally large spin orbit coupling, attributed to the relatively large atomic number of ruthenium.

Chapter 2

SrRuO₃ Thin Films

First, a basic overview of strontium ruthenate: SrRuO₃ (SRO) is an itinerant ferromagnet, with a Curie temperature (T_c) of $\sim 160\text{K}$ in single crystal form [69], and a strain reduced T_c in thin films, typically to $\sim 150\text{K}$ [35]. It is particularly notable for its strong spin orbit coupling and large magnetocrystalline anisotropy as a result. SRO is also a metallic oxide, though it is sometimes referred to as a “bad metal” due to its relatively low conductivity and prevalence of electron-electron correlations. SRO has a perovskite structure, and single crystals of SRO are orthorhombic (and pseudocubic) below 850K. This chapter will discuss in greater detail the physics behind, and the specific details of, the structural, electric, and magnetic properties of SRO.

2.1 Structural Properties of SrRuO₃

SRO is a perovskite, which means that it has a structure analogous to the natural compound CaTiO₃. The chemical formula of a perovskite is ABO₃, and a single unit cell, in the idealized cubic-symmetry structure, can be depicted with the A-site atoms at the corners of a cube, the B-site atom in the center, and the oxygen centered in the faces of the cube in an fcc structure. The idealized cubic structure is shown for SRO in figure 2.1. In perovskites, the oxygen form an octahedron around the B-site atom, and when the structure is not cubic the oxygen octahedra can tilt or rotate.

In single crystals of SRO the structure is cubic above 950K, between about 950 and 850K it distorts slightly into a tetragonal phase and below 850K it is orthorhombic and pseudocubic. In orthorhombic form, the lattice parameters are $a = 5.53 \text{ \AA}$, $b = 5.57 \text{ \AA}$, and $c = 7.84 \text{ \AA}$ [50]. When SRO is grown epitaxially on films its in-plane lattice parameters distort to match the substrate. An additional change can come from the oxygen octahedra, which are rotated about all three orthorhombic axes. This rotation can be described by Glazer notation, which for SRO can be written: $a^-a^-c^+$ [108]. This tells us that the rotation is similar around the a and b axes and distinct around the c axis. The - and + signs indicate that adjacent octahedra are rotated in either the opposite or the same direction. These rotations are depicted for SRO in figure 2.1. Additional changes in thin films include a reduced Curie temperature and higher residual resistivities [17, 52].

SrRuO₃ exhibits the Invar effect, which means that its lattice parameters are nearly

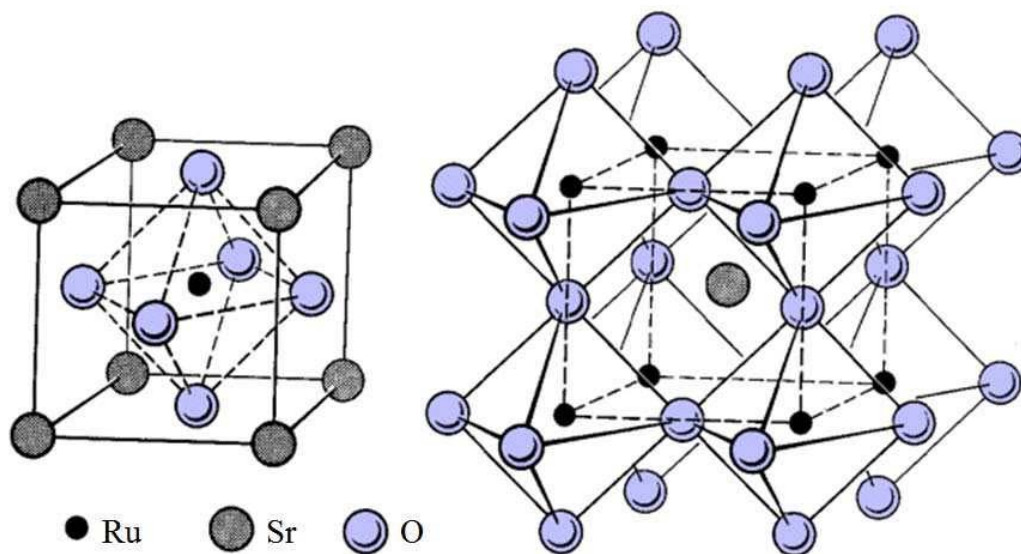


Figure 2.1: Idealized cubic structure of SRO.

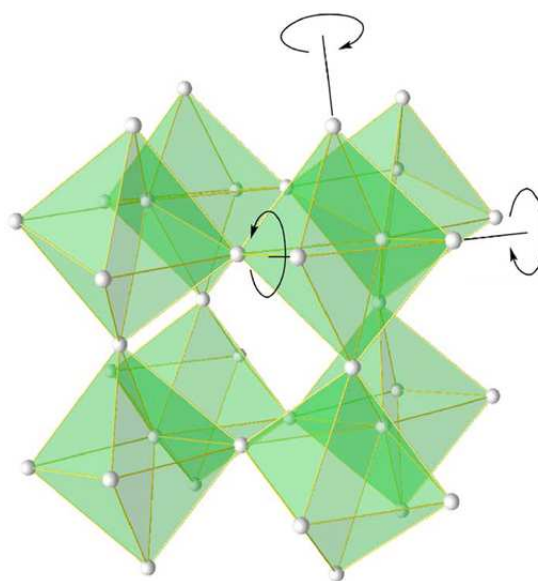


Figure 2.2: Orthorhombic structure of SRO, showing oxygen octahedra rotations. From [108].

constant as a function of temperature. The fractional change in lattice parameter is less than $\frac{\Delta a}{a} \approx 10^{-4}$ between 0 and 300 K [50]. Although, in general, thermal expansion mismatch can result in a temperature dependent strain between a thin film and the substrate it is grown on, this was not observed in any of the SRO films in this thesis.

2.2 Film Growth

Previous optical studies of SRO have been primarily on SRO grown on SrTiO₃ (001) substrates. In this thesis, SRO films were studied in different orientations and on different substrates, as described in the following two sections. Orthorhombic orientations are referred to unless otherwise specified.

2.2.1 Samples for demagnetization experiments

SRO films for the demagnetization experiments were grown via pulsed laser deposition at 700°C in 0.3 mbar of oxygen and argon (1:1) on TiO₂ terminated STO in (111) orientation [62]. A pressed pellet of SRO was used for the target material and the energy on the target was kept constant at 2.1 J/cm². High-pressure reflection high-energy electron diffraction (RHEED) was used to monitor the growth speed and crystallinity of the SRO film in situ. RHEED patterns and atomic force microscopy imaging confirmed the presence of smooth surfaces consisting of atomically flat terraces separated by a single unit cell step (2.2Å in the [111] direction). X-ray diffraction indicated fully epitaxial films and x-ray reflectometry was used to verify film thickness. Bulk magnetization measurements using a SQUID magnetometer indicated a Curie temperature, T_c , of ~155K. The relatively high T_c of the film is indicative of film quality. Electrical transport measurements were performed in the Van der Pauw configuration and show the residual resistance ratio to be about 10 for these films.

2.2.2 Samples for strain experiments

For the strain experiments, thin 10nm films of SRO were grown on several different substrates, including STO, DyScO₃ (DSO), and GdScO₃ (GSO), all in the (001) orientation. Some of the DSO substrates were found to have unusually large in-plane lattice parameters, thought to be due to dysprosium deficiencies. These substrates will be referred to as D_{1-δ}SO.

Structurally, SRO films can grow with either (001) or (110) orientations on substrates with (001) orientation. An illustration of these two geometries can be seen in figure (2.2.2). Further discussion of the orientation of SRO on these substrates will continue in chapter 5.

Pulsed-laser growth of these films was done at 680-700°C in 100 mTorr oxygen, and RHEED, X-ray diffraction, and x-ray reflectometry were again used to ensure film quality and thickness. SQUID measurements showed Curie temperatures of ~150K.

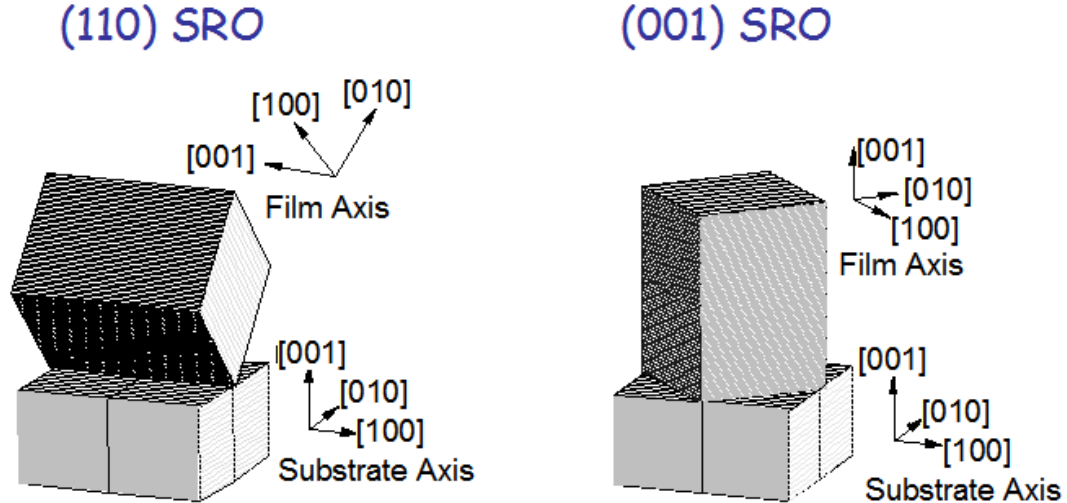


Figure 2.3: Possible orthorhombic orientations of SRO on substrates with (001) orientation. On the left is the (110) orientation, and on the right is the (001) orientation. From [46]

2.3 Electronic Properties

This section will give a brief overview of unusual electronic properties of SRO, as the electronic properties were not the primary focus of this thesis work. Both conductivity and carrier concentration are lower in SRO than in typical metals [52].

2.3.1 Non-Fermi Liquid Behavior in SRO

In the independent electron approximation, electrons are treated as non-interacting particles. At first glance, this simple approximation would seem not applicable to most real systems. The concept behind Fermi Liquid theory is that, even though there may be electron-electron interactions in a system, groups of electrons can be renormalized and treated as non-interacting quasiparticles [71, 4]. Fermi Liquid is surprisingly robust, only failing in the instance of strong electron-electron interactions [73].

Evidence of non-Fermi liquid behavior in SRO comes the high temperature resistivity. At high temperatures, the resistivity of a normal metal is flat, having saturated once the mean free path of electrons becomes less than the interatomic spacing, or de Broglie wavelength. In SRO, the resistivity continues to increase past this point, at $\sim 500\text{K}$ [3, 51, 29, 18].

Further evidence of non-Fermi behavior comes from the IR conductivity, which has non-Drude like frequency dependence at high frequency, and photoemission spectroscopy, which shows a broader Ru 4d band than would be expected from non-interacting band theory [63, 34].

The failure to conform to Fermi liquid behavior suggests strong electron-electron correlations in SRO. These correlations are believed to be the result of the unusual hybridization of Ru 4d electrons with oxygen 2p electrons [65].

2.3.2 Anomalous Hall Effect

In a ferromagnet, the Hall resistivity includes an additional term arising from the magnetization of the material. Called the anomalous Hall effect (AHE), this contribution to the resistivity is analogous to the classic Hall effect, only the off-diagonal term in the conductivity comes from the intrinsic magnetization of the material instead of an applied magnetic field. The full Hall resistivity can be written as a function of temperature and magnetic field, H :

$$\rho_{xy} = R_0(T)H + R_a(T)M(T, H) \quad (2.1)$$

where R_0 is the normal Hall coefficient and R_a is the anomalous Hall coefficient. The AHE arises from the spin-orbit interaction, which couples the magnetization of a ferromagnet to an applied electric current [84, 94].

The origin of the AHE is still under debate [74, 55, 33]. There are two competing theories: 1) The AHE is an extrinsic effect, resulting from asymmetric scattering from impurities [96, 8], and 2) The AHE is an intrinsic band structure effect, which can be described in terms of Berry's phase and is related to magnetic monopoles in momentum space [84, 82, 33, 78].

Calculations by Fang et al. suggest that the intrinsic AHE should be dominated by avoided crossings (near degeneracies) in the band structure, and that the intrinsic AHE should be dominant in SRO [33, 85]. The off-diagonal conductivity can be written [84]:

$$\sigma_{xy}(\omega) = i \sum_{m,n,k} \frac{J_{mn}^x(k)J_{nm}^y(k)f_{mn}(k)}{\epsilon_{nm}(k)[\epsilon_{nm}(k) - \omega - i\gamma]} \quad (2.2)$$

where $J_{mn}^i(k)$ is the current matrix element between quasiparticle states with band indices n , m and wave vector k . The functions $\epsilon_{nm}(k)$ and $f_{nm}(k)$ are the energy and occupation difference, respectively, between such states, and γ is a phenomenological quasiparticle damping rate.

The AHE conductivity is the dc limit of σ_{xy} . Looking at equation (2.2) we see that the size of the intrinsic AHE depends on the position of the Fermi energy with respect to near degeneracies in the band structure. If the Fermi energy lies between two energy bands the difference in the Fermi occupation, $f_{nm}(k)$, will be large. If the energy bands are close together, as in the case of an avoided crossing, the energy difference, $\epsilon_{nm}(k)$, will be small. The intrinsic AHE is most likely to dominate when the Fermi energy lies between, or near, an avoided crossing.

Calculations of the intrinsic AHE have been done using linear response theory [33, 84]. Given the wide spread applicability of this theory, it has been suggested that other physical observables should be related to near degeneracies in the band structure as well, in particular observables related to collective spin dynamics, such as ferromagnetic resonance [83].

2.4 Magnetic Properties

2.4.1 Itinerant Ferromagnetism

Metals, such as SRO, have conduction electrons that are free to move within the material. This is in contrast to electrons which are localized, bound to a particular atom. Magnetism that originates in the traveling conduction electrons is thus said to be “itinerant”. A neat separation between conduction and valence electrons is inaccurate, however. In SRO, itinerant electrons are actually hybridized states of s-p and d electrons.

The saturated magnetic moment of SRO is $\sim 1.6 \mu_B/\text{Ru atom}$, where μ_B is the magnetic moment of a single spin [17]. The magnetization arises from electrons of 4d character associated with the Ru atoms [51]. The non-integer number of Bohr magnetons (μ_B) comprising the magnetic moment cannot be explained by a local picture of magnetism. It is one of the hallmarks of an itinerant ferromagnet, and illustrates the need for a non-local, band description of ferromagnetism [95].

Ferromagnetism arises as the result of a spontaneous splitting between spin up and spin down energy bands. Whether or not spin bands split is determined by a competition between reduced energy as a result of exchange interaction favoring spin alignment with increased kinetic energy due to spin band splitting, as will be discussed in more detail in the next section. As always, nature tries to minimize the energy of the system.

The reduction in energy due to exchange interaction is a result of Coulomb interactions which favor a symmetric spin state. The Pauli exclusion principle favors an overall electron state which is antisymmetric, but that asymmetry can come from either the spatial or the spin portion of the wavefunction. Electrons in an anti-symmetric spatial state are relatively delocalized compared to electrons in a symmetric spatial state. This delocalization means that electrostatic Coulomb energy due to electron-electron interactions is reduced. If the anti-symmetric spatial state is favored, then symmetric spin state must be as well, satisfying the Pauli exclusion principle[98]. Thus the Coulomb interaction gives rise to magnetic ordering. In SRO, exchange is mediated through hybridization of the 4d Ru electrons with 2p O orbitals [65].

2.4.2 The Stoner Model

The Stoner model is a simple band model for itinerant ferromagnetism. In the Stoner model, the energy band of one spin type spontaneously shifts with respect to the other. The result of this shift is that one spin band has more available states below the Fermi energy, as depicted in figure 2.4. Therefore there is a preferential orientation of spin in the system. The net magnetization is determined by the difference between the number of majority and minority spins: $M_{net} = \mu_B(N_{maj} - N_{min})$.

Band splitting will occur if it leads to a reduction in the total energy, where: $\Delta E_{total} = \Delta E_{kin} + \Delta E_{pot}$. When the bands shift, minority spin electrons with total energy just below the original Fermi energy will perform a spin flip and be effectively promoted to a higher kinetic energy. The new total energy will be just above the original Fermi energy in the majority band. This kinetic energy cost depends on the number of spins that flip, in other words, the density of states at the Fermi surface, $g(\mathcal{E}_F)$. The energy cost can only

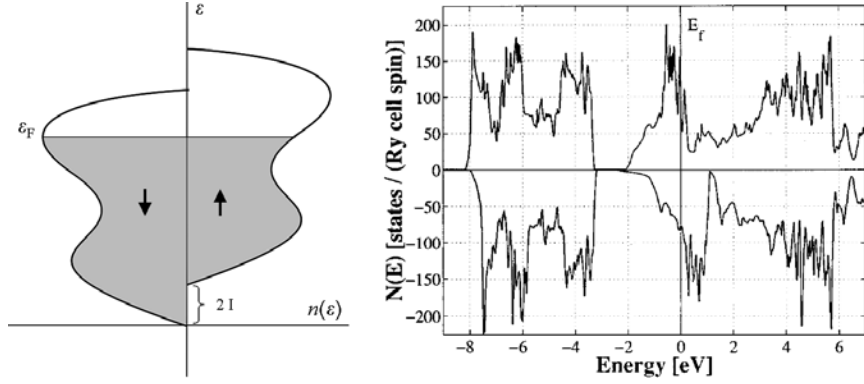


Figure 2.4: Left: Diagram of band shifting in the Stoner Model. \mathcal{E} is total energy: magnetic + kinetic. Right: Calculated density of states for SRO. [3]

be overcome if the potential energy savings from exchange interactions between electrons and the molecular field exceeds the kinetic cost. This condition for spontaneous splitting is represented by the “Stoner criteria” for ferromagnetism:

$$U \cdot g(\mathcal{E}_F) \geq 1 \quad (2.3)$$

where U represents the Coulomb energy, and can be written [37]:

$$U = \mu_0 \mu_B^2 \lambda \quad (2.4)$$

where λ relates the average molecular field felt by each spin, B_{mol} , to the magnetization, M , through: $B_{mol} = \lambda M$, as will be described in more detail in the next section.

If the Stoner criterion is fulfilled, the spin up and spin down bands will split by an energy Δ_{ex} , called the exchange energy. If the criterion is not met, there will be no spontaneous magnetization.

The robustness of a ferromagnet is determined by the size of the exchange energy and the position of the Fermi energy in the majority spin band. Metals which exhibit an exchange splitting greater than the difference between the Fermi energy and the top of the majority spin band are called strong. They have no holes in the majority in spin band. Metals with an exchange splitting less the difference between the Fermi energy and the top of the band are referred to as weak, and are prone to spin flip excitations, since they have holes in both the minority and majority bands. The density of states for SRO, seen at right in figure 2.4, demonstrates an example of a weak ferromagnet.

The Stoner model is flawed, particularly in its inability to explain the temperature dependence of magnetism near the Curie temperature [98, 92]. But the utility of the Stoner model comes from its ability to explain fractional spin magnetic moments and elucidate the criteria by which a material will become ferromagnetic.

2.4.3 Mean Field Theory

A relatively simple model of magnetization that does accurately describe the temperature dependence of ferromagnets near the Curie Temperature (at least in the absence of fluctuations of the order parameter) is Mean Field theory for magnetization, also known as the theory of Weiss.

The magnetically relevant part of the Hamiltonian for a ferromagnet, in the absence of an external field, is given by:

$$H = - \sum_{ij} J_{ij} S_i \cdot S_j \quad (2.5)$$

where all spins are summed over and J_{ij} is the exchange integral between spin i and spin j . The equation would be quite cumbersome to solve exactly, so instead the approximation is made that the interaction of a spin with its neighbors can be described by a uniform, average field, and this field should be proportional to the magnetization. This average field is called the molecular field, B_{mol} :

$$B_{mol} = \lambda M \quad (2.6)$$

The Hamiltonian can then be rewritten in terms of the molecular field:

$$H = g\mu_B \sum_i S_i \cdot B_{mol} \quad (2.7)$$

Making use of the partition function, Z , a transcendental equation satisfying the Hamiltonian can be found:

$$M(T) = M_s B_J \left(\frac{g\mu_B J \lambda M(T)}{kT} \right) \quad (2.8)$$

where M_s is the saturation magnetization, and B_J is the Brillouin function.

Solutions to this equation can be found graphically, as seen in figure 2.5, by plotting both sides of the equation, and looking for points of intersection. There is always the trivial solution to this equation for $M(T) = 0$, and above a certain temperature that is the only solution. T_c is defined by the temperature at which slopes of the sides of the equation become equal, and for temperatures below T_c , three possible solutions exist: $M(T) = 0, \pm M_0$.

Near T_c , and for $J = 1/2$, the magnetization is found to have the following behavior:

$$\frac{M}{M_s} \propto (T_c - T)^{1/2} \quad (2.9)$$

Mean Field Theory has been shown to accurately describe the critical behavior of magnetization in SRO near the Curie temperature down to very small reduced temperatures ($(T_c - T)/T_c$) of 10^{-4} or less [47].

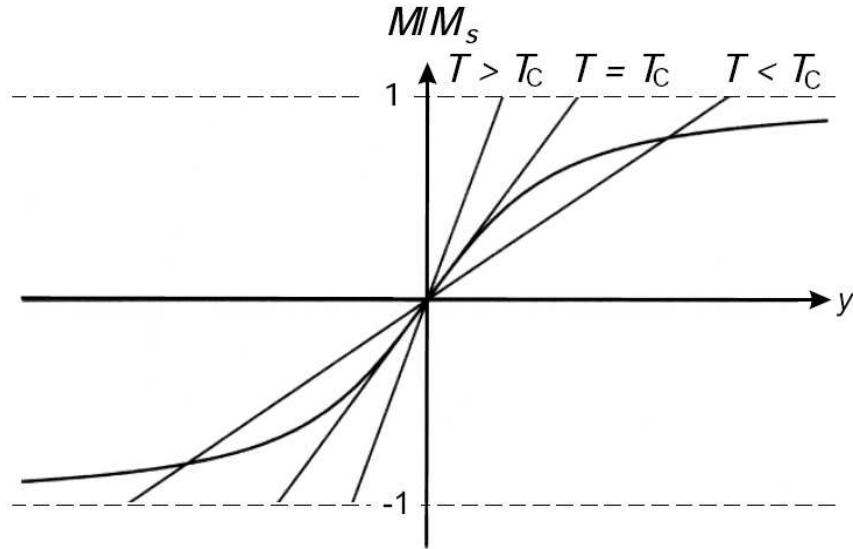


Figure 2.5: Left: Graphical method to determine magnetization from mean field theory. Above T_c there is only one solution, $M = 0$. Below T_c three solutions exist: $M = 0, \pm M_0$ [37]

2.5 Magnetic Anisotropy

In an anisotropic material, the internal energy depends on the direction of the magnetization. The magnetic anisotropy field represents the expression of this directional dependence. The direction of the field indicates the lowest energy position of the magnetization. For a material with uniaxial anisotropy, such as SRO, this is the “easy axis” direction. For a higher symmetry system there could be, for instance, an easy plane. The strength of the field indicates the degree of resistance to movement of magnetization away from the preferred orientation. The most important contributions to the magnetic anisotropy for thin films of SRO are magnetocrystalline anisotropy, shape anisotropy, and anisotropy due to strain (or inverse magnetostriction).

2.5.1 Magnetocrystalline Anisotropy

Magnetocrystalline anisotropy is an intrinsic anisotropy arising from the spin orbit interaction of electrons[44]. Spins prefer to align along particular crystallographic axes due to the close relationship between the electron orbitals and the crystallographic structure [37]. Materials with strong spin orbit coupling, such as SRO, also exhibit large magnetocrystalline anisotropy fields.

Anisotropy arising from intrinsic spin orbit coupling may be uniaxial, but it can't be unidirectional, in the sense that it should be just as easy for the magnetization to align anti-parallel to the anisotropy field as parallel to it. Another way of expressing this idea is to say that the anisotropy energy can be written in terms of even powers of the angle θ

where θ is the angle the magnetization makes with the direction of the anisotropy field [20]:

$$E = K_2 \sin^2 \theta + K_4 \sin^4 \theta + \dots \quad (2.10)$$

Here, the values of the magnetocrystalline anisotropy constants, K_i , determine the behavior of the system. For example, if all $K_i > 0$, the material will exhibit uniaxial anisotropy, and easy plane anisotropy if all $K_i < 0$.

Further discussion of the relationship between the crystallographic symmetry, the magnetocrystalline anisotropy field, and the magnetization direction will be presented in section 3.1.2.

2.5.2 Shape Anisotropy

If a sample of magnetic material is not spherical, preferred orientations of the magnetic field can present themselves based on the shape of the sample, a phenomenon known as shape anisotropy. This phenomenon is caused by the dipole interaction between spins. Each spin feels the dipole field of every other spin in the sample [20]. In the middle of the sample these dipole fields cancel one another, but near the boundaries of the sample these fields are uncompensated. These uncompensated dipoles give rise to a stray field outside the sample which tries to counteract the magnetic field within the sample. This stray field is called the demagnetization field.

Since this field depends on where the boundaries are, the demagnetization energy is shape dependent. For a thin film where the out-of-plane dimension is much smaller than the in-plane dimensions, the stray field energy is given by [44]:

$$E_{str} = \frac{1}{2} \mu_0 M^2 \cos^2 \theta, \quad (2.11)$$

where θ is the angle between the magnetization and the direction normal to a film's surface. The shape anisotropy energy is highest when the spins point out of the plane because the distance between uncompensated dipoles is the greatest in that orientation. In order to minimize the shape anisotropy energy, the shape anisotropy field prefers spins to align in the plane of a film.

2.5.3 Inverse Magnetostriction

Magnetic anisotropy can also arise from strain applied to a material through magneto-elastic interaction. Textbooks typically focus on the opposite of this effect: magnetostriction, an induced strain resulting from changing bond lengths. The bond lengths change to minimize the spin interaction energy, which depends on both the distance between individual magnetic moments and the direction of magnetization [20]. This effect is responsible for the distortion of a cubic lattice into a tetragonal lattice below the Curie temperature of a magnetic material, for example [37]. But an inverse magnetostriction effect, called the Villari effect, is also possible.

Strain arises in films due to the distortion of in-plane lattice parameters to match the substrate [25]. If the layer is grown epitaxially this strain is homogeneous across the sample, and a corresponding distortion occurs normal to the surface of the film. In thick

films, any distortion to the material will relax to bulk values in layers sufficiently far away from the substrate [27]. In the thin films of SRO looked at in the thesis, however, the strain is approximately uniform throughout the sample, except where specifically noted in the case of SRO grown on GdScO_3 . This is only an approximation, though, since the magnetic transition is found to be broader in temperature for films, which indicates non-uniform strain.

Calculations of SrRuO structure suggest strong magneto-structural coupling [108], and the strength of this coupling is evidenced by the reduction in the saturated magnetic moment and lowered transition temperature [35] for SRO films compared to SRO crystals. Notably, this happens even though the strain from lattice mismatch in between SRO and the various substrates it was grown on is relatively small. The reduction in saturated moment means that the magnitude of the anisotropy field has been reduced due to strain.

Magneto-structural changes in SRO correlate to changes in the oxygen octahedra [108]. The oxygen octahedra can rotate or deform in response to strain and in turn induce changes in the position and orientation of associated orbitals. Since magnetocrystalline anisotropy depends on spin-orbit interactions this can change the strength or direction of the anisotropy field. An example of the strong magneto-structural coupling comes the possible quashing of magnetism in SRO with applied strain. The high-spin state of SrRuO_3 is the result of four 4d Ru electrons occupying three degenerate t_{2g} orbitals, which leaves two spins uncompensated. A distortion of the bond lengths in an oxygen octahedron can lift the degeneracy of the t_{2g} orbitals, and a strong distortion can create a low-energy state where the 4 Ru electrons occupy only two orbitals. The result in this case is that there is no net magnetic moment.

Further discussion of the effect of strain on the anisotropy field direction in SRO can be found in section 2.6 and chapter 5.

2.5.4 Anisotropy in SRO

Having discussed possible contribution to magnetic anisotropy, let's direct our attention to the specifics of the anisotropy field in SRO. The anisotropy field is dominated by magnetocrystalline anisotropy, thanks to strong spin orbit coupling. The magnitude of the anisotropy field in SRO is unusually large on account of this, $\sim 6\text{-}7\text{T}$ [72]. The strength of the anisotropy field makes ferromagnetic resonance in SRO appropriate for study with ultrafast techniques, as we shall see. The direction of the anisotropy field is known to rotate in the a-b plane in films [51]. This rotation is shown in figure 2.5.4 for a film of SRO grown on STO. Near the Curie temperature the anisotropy field points along the b-axis of the lattice. Upon cooling, the anisotropy field rotates away from the b axis and toward the a-axis, rotating a total of approximately 15° as temperature approaches zero. For SRO (110), the orientation it grows on STO, this means that near 150K the anisotropy field makes an angle of 45° with the normal to the film surface, and at 5K an angle of 30° .

There is no consensus in the literature regarding whether the anisotropy field rotates in crystals of SRO. But since the anisotropy field rotates toward normal as it is cooled, we know that this rotation cannot be the result of shape anisotropy. If such a rotation were due to shape anisotropy, then as the magnitude of the magnetization increased at low temperature the field would want to align more in-plane to reduce the energy of the

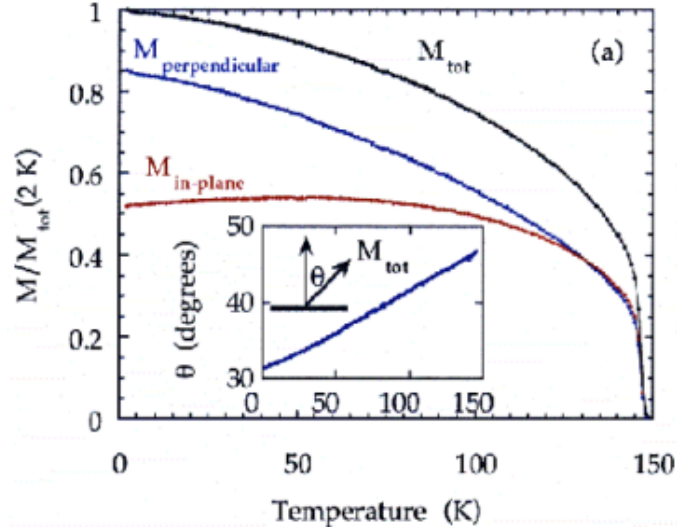


Figure 2.6: In-plane (red), out-of-plane (blue), and total magnetization (black) as a function of temperature. The angle of the easy axis relative to the sample normal is shown in the inset. Figure from [51].

stray field. Instead the rotation is in the opposite direction, and must be caused by the intrinsic magnetocrystalline anisotropy.

The rotation of the magnetocrystalline anisotropy field as a function of temperature can be explained by the relatively simple free energy introduced in equation (2.10). If equation (2.10) can be truncated after $\sin^4 \theta$, and K_2 and K_4 have opposite sign, the direction of the easy axis is determined by $\sin \theta = \sqrt{-\frac{K_2}{2K_4}}$. If K_2 and K_4 vary as a function of temperature, the direction of the anisotropy will rotate as a function of temperature.

Equation (2.10) is equally good for magnetization parallel or anti-parallel to the anisotropy field direction, but experimental results can be washed out or difficult to interpret if both magnetic domains are actually present. Consequently, we used a small permanent magnet with a field of ~ 0.5 T in the cryostat to seed spins along one magnetic domain as we cooled through the transition temperature. Since the magnetic susceptibility diverges near the Curie temperature, only a relatively small field was necessary. We also found that even when the magnetization was saturated at low temperature, a coercive field of less than one tesla was needed to switch from one orientation to another.

2.6 Strain Effects

Having covered the basic properties of SRO, we can now explore structural and magnetic changes to those properties as a function of strain. In this section the focus will be on structural changes, along with motivation for the magnetic changes that will be discussed in chapter 5.

When SRO is grown epitaxially, its in plane lattice parameters are compressed or

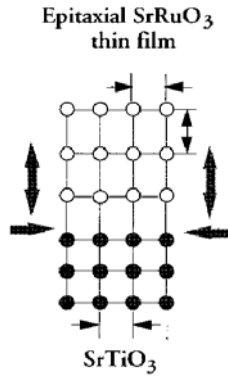


Figure 2.7: Epitaxial growth of SRO on STO. The in-plane lattice parameter is compressed.

stretched to fit the substrate. A corresponding stretch or compression of the out-of-plane lattice parameter is observed such that the unit cell maintains (roughly) its volume. For example, when SRO is grown on STO, its in-plane lattice parameters are compressed and its out-of-plane lattice parameter is stretched, as seen in figure 2.6.

The degree of rotation of the oxygen octahedra also reflects the impact of epitaxial strain. As the lattice parameters distort as a function of strain, the oxygen octahedra will rotate to preserve their shape [108]. Using *ab initio* calculations, the rotation of the oxygen octahedra can be predicted as a function of strain. We see in figure 2.6, for the two possible orientations of SRO growth, a calculation of the expected rotation angle of the octahedra as a function of strain. The data labeled as tilting refers to the rotation corresponding to the a and b directions, and the data labeled rotation refers to the rotation about the c axis. We see that there are significant changes in the rotation as a function of strain and that these changes in the rotation are different for films with different orientations of SRO growth.

The anisotropy field in SRO is fundamentally linked to the oxygen octahedra through the role oxygen 2p electrons (hybridized with ruthenium 4d electrons) play in spin-orbit coupling. The predicted rotation of the oxygen octahedra with strain suggests that we should see correlated changes in the magnetization as a result of this strong magneto-structural coupling.

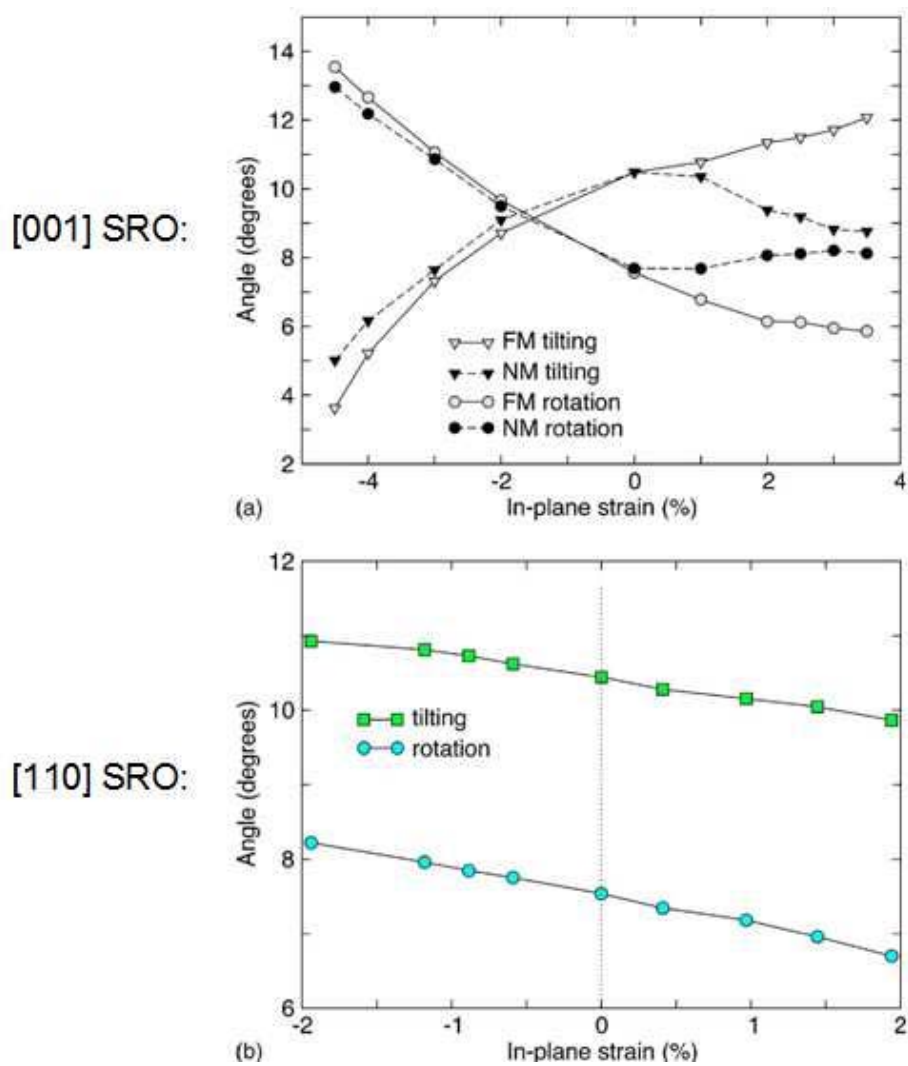


Figure 2.8: Rotation of the RuO_6 octahedra as a function of strain in SRO. The top plot shows the rotation for (001) SRO and the bottom plot shows the rotation for (110) SRO. The relevant calculations in the top plot are labeled 'FM' for ferromagnetic. From [51].

Chapter 3

Ultrafast Magnetization Dynamics

3.1 Theory of Magnetization Dynamics

3.1.1 The Landau-Lifshitz-Gilbert Equation

Understanding magnetization dynamics begins with understanding the dynamic behavior of a single spin. The motion of a spin is determined by the equation of motion, which can be derived from quantum theory [36]. According to quantum mechanics, the time evolution of the expectation value of an operator is determined by the expectation value of its commutation with the Hamiltonian operator H . Hence for a spin \mathbf{S} :

$$-i\hbar \frac{d\langle \mathbf{S} \rangle}{dt} = \langle [\mathbf{S}, H] \rangle \quad (3.1)$$

We would like to understand the motion of a spin in the presence of an external magnetic field. The relevant Hamiltonian, which describes the interaction of the spin with the external field, \mathbf{B} , can be expressed as:

$$H = -\frac{g\mu_B}{\hbar} \mathbf{S} \cdot \mathbf{B} \quad (3.2)$$

where μ_B is the Bohr magneton and g is the g-factor for a free electron.

With the aid of the commutation rules for spin operators [83]:

$$[S_i, S_j] = i\hbar \epsilon_{ijk} S_k \quad (3.3)$$

where ϵ_{ijk} is positive one for right-handed permutations of x,y, and z, and negative for left-handed permutations, the spin equation of motion can be found:

$$\frac{d\langle \mathbf{S} \rangle}{dt} = \frac{g\mu_B}{\hbar} (\langle \mathbf{S} \rangle \times \mathbf{B}) \quad (3.4)$$

The derived equation of motion for one spin can be extended to the macroscopic level for the case of homogeneous magnetization, considering the relationship between the magnetization \mathbf{M} and $\langle \mathbf{S} \rangle$:

$$\mathbf{M} = \frac{g\mu_B}{\hbar} \langle \mathbf{S} \rangle \quad (3.5)$$

The analogous equation of motion for magnetization in an external field \mathbf{H} is:

$$\frac{d\mathbf{M}}{dt} = -\gamma\mu_0 (\mathbf{M} \times \mathbf{H}) = \gamma_0 (\mathbf{M} \times \mathbf{H}) \quad (3.6)$$

where $\gamma = g\mu_B/\hbar$ is called the gyromagnetic ratio, and $\gamma_0 = -\gamma\mu_0$. Consider an array of homogeneous magnetic moments comprising the magnetization in a sample. Equation (3.6) describes the torque that the magnetic moments collectively feel in response to an external field. The torque changes the angular momentum of all of those magnetic moments, resulting in the coherent precessional motion of the spins.

Inspection of equation (3.6) reveals that, by virtue of the cross product between \mathbf{M} and \mathbf{H} , the precessional motion has certain properties in the case of a constant external field \mathbf{H} :

$$\frac{d}{dt}(\mathbf{M})^2 = 0 \quad \frac{d}{dt}(\mathbf{M} \cdot \mathbf{H}) = 0 \quad (3.7)$$

This implies two things: First, that the amplitude of the magnetization is unchanged during precession around a constant field, and, second, that the magnetization, once taken out of the equilibrium position, will precess with the Larmor frequency $\omega_L = \gamma_0 H$ around \mathbf{H} at a fixed angle, for an infinitely long time. This second result is unphysical, since the experimental observation is that the magnetization eventually aligns with the external field. Solving this problem requires the introduction of a phenomenological dissipative term into equation (3.6). Since the dissipative term must serve to align the magnetization with the external field, it is sensible that it be proportional to the cross product of the magnetization and the precessional term. Landau and Lifshitz introduced such a term in the Landau-Lifshitz equation [13, 98]:

$$\frac{d\mathbf{M}}{dt} = \gamma_0 [\mathbf{M} \times \mathbf{H}] + \frac{\alpha\gamma_0}{|\mathbf{M}|} [\mathbf{M} \times (\mathbf{M} \times \mathbf{H})] \quad (3.8)$$

where α denotes the dimensionless damping parameter.

The Landau-Lifshitz equation works well for small values of the damping parameter, but is inaccurate when α is of order one or more. A better description is given by adding a higher order term in α , yielding the Landau-Lifshitz-Gilbert equation:

$$(1 + \alpha^2) \frac{d\mathbf{M}}{dt} = \gamma_0 [\mathbf{M} \times \mathbf{H}] + \frac{\alpha\gamma_0}{|\mathbf{M}|} [\mathbf{M} \times (\mathbf{M} \times \mathbf{H})] \quad (3.9)$$

where α is now referred to as the Gilbert damping parameter.

This is frequently re-written as:

$$\frac{d\mathbf{M}}{dt} = \gamma_0 [\mathbf{M} \times \mathbf{H}] + \frac{\alpha}{|\mathbf{m}|} \left[\mathbf{M} \times \frac{d\mathbf{M}}{dt} \right] \quad (3.10)$$

The Landau-Lifshitz-Gilbert (LLG) equation describes the damped precessional motion of magnetization in the presence of an external magnetic field. If the external field applying the torque is constant, the dissipation time is $\tau_{LLG} = 1/\omega_L \alpha$.

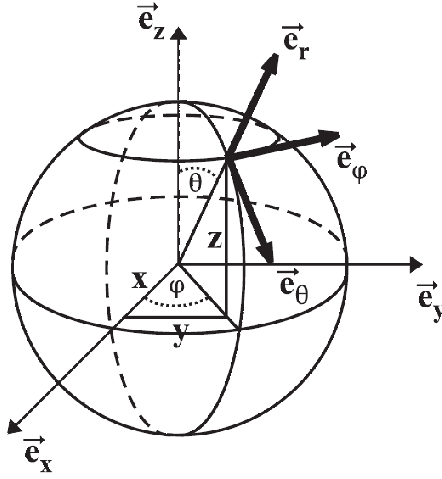


Figure 3.1: Schematic of spherical coordinates.

Applying an external magnetic field is a straightforward way to induce a dynamic response in a magnetic material but, as will be explained in section 4.1, laser excitation can also be used to excite spin dynamics.

3.1.2 Determining Magnetization Dynamics from the Free Energy Potential

In a ferromagnet, the magnetization dynamics are determined by the effective anisotropy field \mathbf{H}_{eff} in the sample [97]. Ignoring the damping term, the magnetization dynamics are determined by the cross product of the magnetization with the effective anisotropy field:

$$\frac{d\mathbf{M}}{dt} = -\gamma\mu_0 (\mathbf{M} \times \mathbf{H}_{eff}) \quad (3.11)$$

The anisotropy field is determined by the derivative of the free magnetic energy, F , with respect to the direction of the magnetization.

$$\mathbf{H}_{eff} = -\frac{1}{\mu_0 M_s} \frac{\partial F}{\partial \mathbf{m}} \quad (3.12)$$

where M_s is the saturation magnetization and \mathbf{m} is the magnetization unit vector.

It is convenient to express equation (3.11) in spherical coordinates, which are schematically shown in figure 3.1.2. Rewriting both sides of (3.11), we find equations that govern the magnetization motion:

$$\frac{d\theta}{dt} = -\frac{\gamma}{M_s \sin(\theta)} \frac{\partial F}{\partial \phi} \quad (3.13)$$

$$\frac{d\phi}{dt} = \frac{\gamma}{M_s \sin(\theta)} \frac{\partial F}{\partial \theta} \quad (3.14)$$

Note in particular that motion in the θ direction is determined by the derivative of the free energy potential with respect to ϕ and vice versa.

The effective anisotropy field is oriented in such a way that all contributions to the free magnetic energy are minimized. Mathematically, this means that \mathbf{H}_{eff} is determined by the minimum of the free energy potential.

The free energy potential can generally be described by a power series expansion of the components of the magnetization, keeping only the even terms, since there is no difference in energy for an oppositely oriented system [37].

$$F = F_0 + \sum_{ij} b_{ij} \alpha_i \alpha_j + \sum_{ijkl} b_{ijkl} \alpha_i \alpha_j \alpha_k \alpha_l + \mathcal{O}(\alpha^6) \quad (3.15)$$

$$F(\mathbf{M}) = F(-\mathbf{M}) \quad (3.16)$$

where the α are the direction cosines, i.e. $\mathbf{m} = (\alpha_1, \alpha_2, \alpha_3)$.

The free energy potential is closely related to the symmetry of the crystal lattice. In the cubic case, the anisotropy axis must always be along a high symmetry axis, such as a lattice vector or a body diagonal, where the particular orientation depends on the sign and value of K_4 and K_6 , magnetocrystalline anisotropy constants which depend on the coefficients b .

$$F = \kappa_0 + \kappa_4(\alpha_1^2 \alpha_2^2 + \alpha_1^2 \alpha_3^2 + \alpha_2^2 \alpha_3^2) + \kappa_6(\alpha_1^2 \alpha_2^2 \alpha_3^2) + \dots \quad (3.17)$$

Since we know that SRO films can rotate as a function of temperature, the cubic case is clearly not enough to describe the symmetry of our system. In the tetragonal case the symmetry restrictions are relaxed a bit and we see that the anisotropy direction is allowed to rotate if κ_2 and κ_4 vary as a function of temperature.

$$F(\theta, \phi) = \kappa_0 + \kappa_2 \sin^2(\theta) + \kappa_4 \sin^4(\theta) + \mathcal{L}_4 \sin^4(\theta) \cos(4\theta) \quad (3.18)$$

where the angle of \mathbf{H}_{eff} is determined by $\sin^2(\theta) = -\kappa_2/2\kappa_4$. We can also see that the ϕ term reflects the four fold symmetry of the basal plane in a tetragonal lattice.

In general the free energy can be quite complicated, given a sufficient lack of symmetry. But for a very small perturbations, such is the case in the experiments discussed in this thesis, the free energy can be expanded in a Taylor series, keeping only terms to second order.

$$F(\theta, \phi) = \kappa_2 \theta^2 + \mathcal{L}_2 \phi^2 + \mathcal{M}_2 \theta \phi \quad (3.19)$$

Given a judicious rotation of coordinates, the cross term can be eliminated.

Now let's focus on magnetization dynamics that result from these free energy potentials. For the cubic case:

$$\frac{d\theta}{dt} = 0 \quad \frac{d\phi}{dt} = \omega_\phi(\theta) \quad (3.20)$$

the resulting motion will be circular. This is true whenever the free energy potential depends only on either θ or ϕ .

But even in the relatively high symmetry of a tetragonal lattice, this is no longer the case:

$$\frac{d\theta}{dt} = f(\theta, \phi) \qquad \frac{d\phi}{dt} = f(\theta, \phi) \qquad (3.21)$$

and the resulting motion is non-circular. In general, if the free energy potential depends on both θ and ϕ the resulting motion will be elliptical. This is easy to see in our case where the perturbation from equilibrium is small:

$$\frac{d\theta}{dt} \sim \mathcal{L}_2\phi \qquad \frac{d\phi}{dt} \sim \kappa_2\theta \qquad (3.22)$$

The solution to these equations of motion are generalized equations for elliptical motion. Including damping:

$$\theta = \theta_A e^{-i\omega t} e^{-t/\tau} + \theta_0 \qquad \phi = \phi_A e^{-i\omega t} e^{-t/\tau} + \phi_0 \qquad (3.23)$$

where τ is the damping time, θ_A and ϕ_A denote the amplitude of those precessions, and θ_0 and ϕ_0 are the equilibrium values of θ and ϕ .

For the time-resolved measurements of magnetization dynamics to be discussed in chapter 5, motion is initiated through a sudden change in the equilibrium position resulting from a change in anisotropy coefficients in response to the laser pulse.

3.2 Damping

Damping of magnetization dynamics can originate from a number of different physical sources. The common thread which unites these effects is that they remove energy and angular momentum from the system, or transfer it to different modes.

A convenient way of breaking down damping is between intrinsic and extrinsic effects.

3.2.1 Intrinsic Damping

Intrinsic sources of damping include eddy currents, phonon drag, and spin-orbit effects such as the one described by the breathing Fermi surface model.

Eddy currents: The changing magnetic field of precessing magnetization creates current in surrounding itinerant electrons due to Faraday's law. This current creates an induced magnetic field that opposes the precessing magnetization due to Lenz's law. Resistive current losses plus the opposing magnetic field result in a damping of the magnetization dynamics. This type of damping is typically distinguished by its temperature dependence which is the same as that of the electrical conductivity. The damping is also proportional to the film thickness squared, and is negligible in thin films ≤ 10 nm.

Phonon Drag: Magnetization dynamics can be damped by direct magnon-phonon scattering, resulting in shear waves. But the damping due to magnetoelasticity is only appreciable if the excited elastic wave can establish a resonant mode based on the

thickness of the film at a corresponding frequency close to that of the precessional motion. The long wavelengths of would-be resonant modes makes them difficult to establish in thin films[40].

Spin-Orbit Effects: In metallic ferromagnets the largest contribution to the damping is thought to be from intrinsic spin-orbit coupling. Two mechanisms which have been proposed are s-d exchange interaction, and a more general approach based on spin-orbit Hamiltonian.

In the s-d exchange interaction, the interaction between itinerant s-p electrons and localized d-spins is considered[41] (though the concept that there are separate conduction and valence electrons is essentially a false premise). Magnons and itinerant electrons are scattered by the s-d exchange interaction, resulting in the creation and annihilation of electron-hole pairs. Only the total angular momentum in the s-d exchange interaction is conserved, and as a result an itinerant electron can spin-flip during scattering with magnons. This scattering by itself does not lead to magnetic damping for the uniform mode of magnons in traditional ferromagnetic resonance experiments (with $q = 0$). The coherent scattering of magnons with itinerant electrons has to be in tandem with incoherent scattering with other excitations, such as thermally excited phonons and magnons. In that case the result is a fast fluctuating torque and magnetic relaxation. The s-d exchange interaction is thought to contribute significantly to Gilbert damping only if the spin flip time is ≤ 50 fs[40].

Damping due to spin-orbit coupling can also be treated more generally using the spin-orbit interaction Hamiltonian[45]. Here, the damping is calculated using the Kubo Green function formalism in the Random Phase Approximation, and can be written[40]:

$$\alpha \propto \int d\mathbf{k}^3 \sum_{\alpha, \beta, \sigma} \langle \beta | L^+ | \alpha \rangle \langle \alpha | L^- | \beta \rangle \delta(\epsilon_{\alpha, \beta, \sigma} - \epsilon_F) \hbar \omega \times \frac{\hbar / \tau_m}{(\hbar \omega + \epsilon_{\alpha, \mathbf{k}, \sigma} - \epsilon_{\beta, \mathbf{k} + \mathbf{q}, \sigma})^2 + (\hbar / \tau_m)^2} \quad (3.24)$$

where τ_m , is the phenomenological momentum relaxation time, the time it takes for electron-hole pairs to recombine. \mathbf{q} is the spin-wave momentum, σ is the electron spin, and the electron bands are represented by α and β .

The damping parameter is either proportional or inversely proportional to the relaxation time depending on the ratio of \hbar / τ_m to the difference in energy bands. for a metallic ferromagnet such as SRO, this difference in energy bands is small and this ratio should be high. This means that the damping parameter should be proportional to the relaxation time, and that the temperature dependence of the damping should scale with conductivity. Also, as with the anomalous Hall effect, the damping parameter should be dominated by near degeneracies in the band structure[61].

The physical picture, when \hbar / τ_m is much larger than energy gap is called the Fermi Breathing Surface Model. The Fermi surface changes with the direction of the magnetization[45]. During precession of the magnetization the Fermi surface distorts periodically in time and space. This periodic distortion is why the Fermi surface is said to be

“breathing”. Electrons repopulate the changing Fermi surface after a time delay caused by their finite relaxation time. This results in a phase lag between the Fermi surface distortions and the precessing magnetization. The damping is proportional to τ_m , because with a greater phase difference, the Fermi surface has time to change more.

When the the energy gap is much larger than \hbar/τ_m , as it can be in interband scattering, the damping parameter is proportional to the inverse of the relaxation time. This means that the temperature dependence of interband scattering should scale with the resistivity, at least at low temperature. At higher temperatures the energy gap is often of the same order as \hbar/τ_m . The physical picture behind interband transitions comes from changes to the electron wave functions not related to changes in energy, such as dynamic orbital polarization[40].

3.2.2 Extrinsic damping

Extrinsic sources such as impurities and structural irregularities can also lead to damping.

Impurities: Defects in the lattice can allow modes to couple which would otherwise not. For instance, spin-waves modes can be coupled by inhomogeneities in the system allowing energy transfer between the uniform mode and higher order modes through scattering. Though the transferred energy is still in the system, the uniform precession is damped[68].

‘Dry friction’: Damping can also occur due to irregularities in the direction of the anisotropy[6]. If individual spins spiral into anisotropies not parallel to the anisotropy felt by the uniform precession, they must be pulled back into the precession by the exchange interaction. Again this represents a transfer of energy away from the uniform precession. This is called ‘dry magnetic friction’, since this type of damping occurs even if the precession is arbitrarily slow. Dry magnetic friction contributes to the damping when the anisotropy is relatively strong in comparison to the exchange coupling.

3.3 Theory of Ultrafast Demagnetization

Demagnetization refers to the loss of magnetization as a result of laser excitation. Early measurements of demagnetization were on the time scale of nanoseconds [103, 2], leading to the popular belief that demagnetization due to laser heating was caused by spin-lattice relaxation. In 1996 Beaurepaire et al. first utilized the time-resolve magneto-optical Kerr effect technique to measure magnetization dynamics in nickel thin films [7]. They observed a reduction in the magnetization on a sub-picosecond time-scale in response to the pump pulse. Since then most elementary ferromagnets have been shown to demagnetize in ~ 100 fs [60]. According to the three temperature model (which will be outlined later) spin-lattice relaxation cannot be responsible for demagnetization on this timescale [7]. Since then demagnetization has been typically attributed to electron-phonon scattering by the Elliot-Yafet mechanism, but is still not well understood from a microscopic perspective. Recently, it has been proposed that electron-electron scattering could result in demagnetization through the Elliot-Yafet mechanism as well, at least in the case of interband scattering at high energies [64].

In the following sections, a few models of demagnetization will be discussed after a brief explanation of the Elliot-Yafet mechanism.

3.3.1 The Elliott-Yafet Mechanism

When an electron undergoes an angular momentum altering event, such as scattering from a phonon, impurity, or another electron, the spin state can change under certain circumstances. One mechanism by which a spin flip can occur is called the Elliot-Yafet mechanism, and is the result of spin up or spin down eigenstates no longer being momentum eigenstates of the system. The physical origin of this effect comes the spin-orbit interaction which lifts the degeneracy of the spin states. The good quantum states are then linear combinations of the spin up and spin down states, and scattering can lead to spin-mixing [21, 109].

The Elliot-Yafet mechanism leads to a spin flip time linearly proportional to the momentum scattering time [28]. In metals, this is expected to be the main spin scattering mechanism.

3.3.2 Three Temperature Model

When Beaurepaire et al. first reported ultrafast laser-induced demagnetization, they interpreted their result in terms of a phenomenological three temperature model (3TM)[7]. This model describes heat flow between electron, lattice, and spin thermal reservoirs, which are assumed to be in internal equilibrium.

The coupled equations for heat flow can be written in terms of the electron temperature, T_e , the lattice temperature, T_L , the spin temperature, T_s , the coupling constants, G , between each bath, and the respective heat capacities and thermal conductivities, C and κ [101, 110]:

$$\begin{aligned} C_e(T_e)\frac{\partial T_e}{\partial t} &= \frac{\partial}{\partial z} \left[\kappa_e(T_e)\frac{\partial T_e}{\partial z} \right] - G_{eL}(T_e - T_L) - G_{es}(T_e - T_s) + S(z, t) \\ C_s(T_s)\frac{\partial T_s}{\partial t} &= \frac{\partial}{\partial z} \left[\kappa_s(T_s)\frac{\partial T_s}{\partial z} \right] - G_{sL}(T_s - T_L) - G_{es}(T_s - T_e) \\ C_L(T_L)\frac{\partial T_L}{\partial t} &= \frac{\partial}{\partial z} \left[\kappa_L(T_L)\frac{\partial T_L}{\partial z} \right] - G_{sL}(T_L - T_s) - G_{eL}(T_e - T_L) \end{aligned} \quad (3.25)$$

where $S(z, t)$ represents the source term from the laser which only couples directly to electrons and \hat{z} is the direction into the sample, perpendicular to the film surface. For thin films lateral heat flow can be neglected. Heat enters the system through the electrons and eventually is passed around to the spins. As the spins heat up, demagnetization occurs.

Since electron-lattice coupling arises from Coulomb interactions, the coupling between the two is thought to be relatively strong in metallic systems. As a result, it is generally expected that electron-lattice thermalization will occur faster than thermalization between electrons and spins, which interact due to spin orbit coupling. Temperature exchange between spins and the lattice is usually attributed to spin-wave interactions with phonons and is thought to be weak, although there is some evidence of magnon-phonon

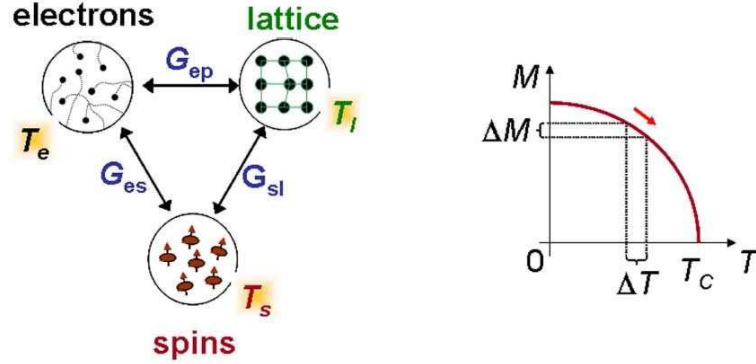


Figure 3.2: On the left, a schematic representation of the three temperature model. On the right, an increase in spin temperature leads to a reduction of the total magnetization. Figure from [23]

coupling in SRO [48]. A domination of spin-electron coupling over spin-lattice coupling is required to explain demagnetization times on the order of 100 fs.

Parameters can always be chosen such that the 3TM will describe demagnetization in a given case, but the sheer number of parameters prevents them from being constrained without a number of assumptions being made.

3.3.3 Koopmans' Model

Recently, Koopmans et al. have built upon the three temperature model with a model which is also phenomenological, but which has the important addition of tracking angular momentum in addition to heat flow [58, 57, 23]. The basis for their model is the assumption that the electron spin is transferred to the lattice via electron-phonon or electron-impurity scattering processes accompanied by spin flip events with a finite probability. They consider a two spin state system split by the exchange energy, Δ_{ex} , and then calculate the transition rate between spin at an initial and final temperature using Fermi's golden rule. They essentially derive equations for coupling constants in the three temperature model based on parameters such as the density of electrons, phonons, and spins, the electron-phonon scattering rate, and the probability of spin flip at a scattering event. What follows is a brief sketch of their theory.

In the mean field theory model of Weiss, for $S_z = \pm 1/2$, the average spin moment, S , can be written:

$$2S = \frac{1 - e^{-\frac{\Delta_{ex}}{k_B T}}}{1 + e^{-\frac{\Delta_{ex}}{k_B T}}} = -\tanh\left(\frac{\Delta_{ex}}{2k_B T}\right) \quad (3.26)$$

The demagnetization time, τ_M , obeys:

$$\tau_M = \frac{\Delta S}{\dot{S}(0)} \quad (3.27)$$

where ΔS is the total change in spin from initial to final temperature, and $\dot{S}(0)$ is the initial change in the time derivative of the spin. \dot{S} is calculated using Fermi's golden rule.

The total change in spin from initial to final temperature is calculated by taking the derivative with respect to T and multiplying by ΔT_e :

$$\Delta S = \left. \frac{dS}{dT} \right|_{T=T_0} \Delta T_e \quad (3.28)$$

and the initial change in the time derivative of the spin can be found similarly:

$$\dot{S}(0) = \left. \frac{d\dot{S}}{dT} \right|_{T=T_0} \Delta T_e \quad (3.29)$$

where the electron temperature increase ΔT_e is calculated at $t = \infty$ if the demagnetization time is much longer than the electron-phonon thermalization time and at $t = 0$ if the opposite is true.

In either limit, the demagnetization time, well below T_c , is found to be:

$$\tau_M = \frac{1}{4} \frac{\hbar}{k_B T_c} \frac{1}{\alpha} \quad (3.30)$$

Preliminary analysis indicates that this equation is in rough agreement with experimental results for a wide range of demagnetization time scales.

Chapter 4

Experimental Technique

4.1 Initiating Demagnetization and Magnetic Precession in SrRuO₃

The dynamics of spins in films of SRO have been studied after excitation by an ultrafast (< 100 fs) laser pulse. The laser excites a small number of electrons through direct ($k = 0$) dipole transitions. These electrons are excited with an energy of 1.5 eV, which is determined by the wavelength of the laser light, 800 nm, through $E = hc/\lambda$. 1.5 eV is orders of magnitude larger than the thermal energy, so at very short times equilibrium concepts of temperature do not apply[60]. Since SRO is metallic, there are many available states near the Fermi energy and electron-electron scattering occurs rapidly. Within a few hundred femtoseconds the initially excited electrons create a bath of “hot” electrons. Once a bath of heated electrons is created in the system, energy can transfer more efficiently from electrons to phonons through electron-phonon scattering, and the lattice temperature comes into equilibrium with the electron temperature in < 1 ps[99, 59].

A reduction in the magnetization is observed in response to the laser pump pulse, with varying timescale. Demagnetization on the time scale of a hundred femtoseconds to tens of picoseconds is thought to be the result of the spin-flip of an electron due to a momentum altering event. Typically this Elliott-Yafet type scattering is attributed to scattering with a phonon or impurity. Previous work has shown that demagnetization can be on the time scale of the initial decay of electrons, suggesting electron-electron spin-flip scattering can also play a role[7, 57].

In SRO, the mechanism for initiating magnetic precession is the thermal excitation of the lattice. The absorption of the pump pulse creates a thermally excited region. Since the angle of the anisotropy field is temperature dependent, this causes a sudden shift in the easy axis direction. The magnetization subsequently spirals in toward the new position as governed by the Landau-Lifshitz Gilbert equation, precessing at its ferromagnetic resonance frequency. This is shown schematically in figure 4.1. As we shall see later, this behavior is manifest as decaying oscillations by the time resolved magneto-optical Kerr effect.

The time resolved magneto-optical Kerr effect has been shown previously to be a capable probe of both demagnetization and ferromagnetic resonance[80, 66] and was the primary experimental technique used in this thesis. In the following section the physics of

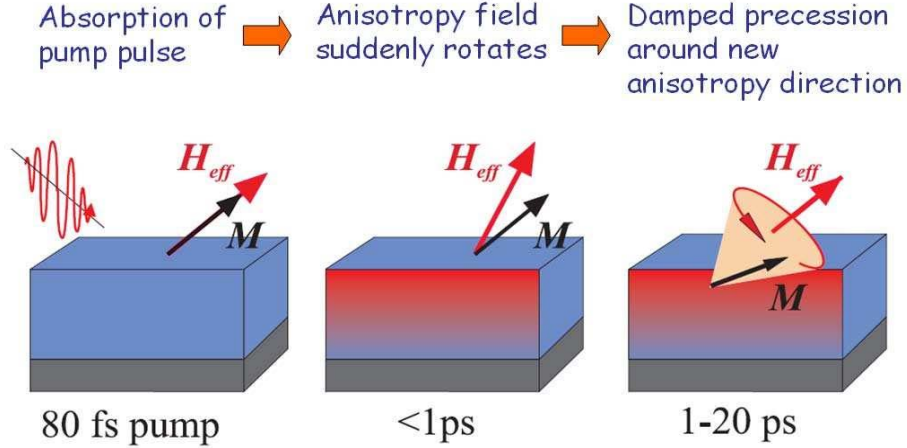


Figure 4.1: Schematic of thermally induced magnetic precession.

the Kerr effect will be discussed and later the experimental implementation will be detailed.

4.2 The Magneto-Optical Kerr Effect

When light is incident on a magnetized material, the interaction between the light and the magnetization of the material results in a rotation of the plane of polarization of the light, proportional to the strength of the magnetization. In reflection, this effect is called the magneto-optical Kerr effect; in transmission, it is called the Faraday effect. The change in polarization originates from time-reversal symmetry breaking due either to an applied magnetic field or spontaneous magnetic ordering, as in a ferromagnet. Time-reversal symmetry breaking can be described as the breaking of symmetry between left and right handedness. This handedness creates a difference in the refractive index, and hence optical absorption coefficients, for right and left circularly polarized light, resulting in a rotation of the polarization.

4.2.1 Phenomenological Description

The phenomenological origin of MOKE is found by incorporating symmetry arguments into the dielectric tensor, $\epsilon(\omega)$, which determines the optical response of a material. The dielectric tensor relates the response of a material, \mathbf{D} , to an external electric field, \mathbf{E} , through:

$$\mathbf{D} = \epsilon_0 \epsilon(\omega) \mathbf{E} \quad (4.1)$$

where \mathbf{D} is called the dielectric displacement vector.

Maxwell's equations in matter are obtained from the equations in free space through the replacement of ϵ_0 with $\epsilon_0 \epsilon(\omega)$. The wave equation describing the propagation of an electric field through a material becomes:

$$\nabla \times (\nabla \times \mathbf{E}) = -\mu_0 \epsilon_0 \epsilon(\omega) \frac{\partial^2 \mathbf{E}}{\partial t^2} \quad (4.2)$$

The dielectric tensor $\epsilon(\omega)$ can be decomposed into a symmetric and anti-symmetric parts[89]. The symmetric part of $\epsilon(\omega)$ does not break time-reversal symmetry, and thus does not contribute to magneto-optical effects. So without loss of generality, only odd, time-reversal breaking contributions to the off-diagonal elements of the dielectric tensor are considered[93]:

$$\epsilon_{ij}(\mathbf{M}, \omega) = \epsilon_{ji}(-\mathbf{M}, \omega) \quad (4.3)$$

An expression for the Kerr effect is derived in reference [106] for light of arbitrary angle of incidence, and an isotropic material ($\epsilon_{xx} = \epsilon_{yy} = \epsilon_{zz}$), where the only symmetry breaking comes from the magnetization of arbitrary orientation. Ignoring quadratic and higher order terms, the dielectric tensor can be written:

$$\epsilon(\mathbf{M}, \omega) = \epsilon_{xx} \begin{pmatrix} 1 & -iQm_z & iQm_y \\ iQm_z & 1 & -iQm_x \\ -iQm_y & iQm_x & 1 \end{pmatrix} \quad (4.4)$$

where $Q = i\epsilon_{xy}/\epsilon_{xx}$ is the magneto-optical constant and the m_i represent the direction cosines of the magnetization \mathbf{M} . Note that the diagonal elements are independent of the magnetization, and the off-diagonal elements transform anti-symmetrically with time reversal, i.e. they change sign when \mathbf{M} is reversed, and they are related to the magnetization.

The expression for the Kerr effect is derived from the Fresnel reflection matrix, \mathfrak{R} . Solving Maxwell's equations for the dielectric tensor given by (4.4), the magneto-optical Fresnel reflection matrix is as follows:

$$\mathfrak{R} = \begin{pmatrix} r_{pp} & r_{ps} \\ r_{sp} & r_{ss} \end{pmatrix} \quad (4.5)$$

where each Fresnel coefficient, r_{ij} , is the ratio of incident j polarized electric field to reflected i polarized electric field, and expressed by:

$$\begin{aligned} r_{pp} &= \frac{n_1 \cos \theta_0 - n_0 \cos \theta_1}{n_1 \cos \theta_0 + n_0 \cos \theta_1} - \frac{i2n_0 n_1 \cos \theta_0 \sin \theta_1 m_x Q}{n_1 \cos \theta_0 + n_0 \cos \theta_1} \\ r_{sp} &= \frac{in_0 n_1 (m_y \sin \theta_1 + m_z \cos \theta_1) Q}{(n_1 \cos \theta_0 + n_0 \cos \theta_1)(n_0 \cos \theta_0 + n_1 \cos \theta_1) \cos \theta_1} \\ r_{ps} &= -\frac{in_0 n_1 (m_y \sin \theta_1 - m_z \cos \theta_1) Q}{(n_1 \cos \theta_0 + n_0 \cos \theta_1)(n_0 \cos \theta_0 + n_1 \cos \theta_1) \cos \theta_1} \\ r_{ss} &= \frac{n_0 \cos \theta_0 - n_1 \cos \theta_1}{n_0 \cos \theta_0 + n_1 \cos \theta_1} \end{aligned} \quad (4.6)$$

where the refractive index of the initial and final mediums are n_0 and n_1 , respectively, θ_0 is the angle of the incidence, and θ_1 is the refractive angle.

The complex Kerr angles, for light initially s or p polarized, are defined as:

$$\theta_K^P = \frac{r_{sp}}{r_{pp}} \qquad \theta_K^S = \frac{r_{ps}}{r_{ss}} \quad (4.7)$$

The equation for the Kerr angle can be simplified considerably in certain circumstances. In order to understand how the off-diagonal components of the dielectric tensor generate the magneto-optical effects, it is useful to consider a simple geometry. In the straight-forward polar Kerr configuration, the most frequently utilized experimental geometry, the light propagates along the direction of magnetization, normal to the material surface. This can be expressed in equation (4.4) as $m_z = 1$, $m_x = m_y = 0$. Due to the nature of time-reversal breaking, the direction that the polarization rotates depends on whether the magnetization is parallel or anti-parallel to the light propagation.

The dielectric tensor for polar Kerr simplifies to:

$$\epsilon(\mathbf{M}, \omega) = \begin{pmatrix} \epsilon_{xx} & \epsilon_{xy} & 0 \\ -\epsilon_{xy} & \epsilon_{xx} & 0 \\ 0 & 0 & \epsilon_{xx} \end{pmatrix} \quad (4.8)$$

Using this expression for the dielectric tensor, and recalling that for polar Kerr light propagates along the magnetization direction ($\mathbf{k} \parallel \mathbf{M}$) and $E_z = 0$, the wave equation for the electric field of the light (4.2) can be written in matrix form:

$$\begin{pmatrix} \epsilon_0 \mu_0 \omega^2 - \epsilon_{xx} & -\epsilon_{xy} \\ \epsilon_{xy} & \epsilon_0 \mu_0 \omega^2 - \epsilon_{xx} \end{pmatrix} \begin{pmatrix} E_x \\ E_y \end{pmatrix} = 0 \quad (4.9)$$

and diagonalized as:

$$\begin{pmatrix} \epsilon_{xx} + i\epsilon_{xy} & 0 \\ 0 & \epsilon_{xx} - i\epsilon_{xy} \end{pmatrix} \begin{pmatrix} E_x + iE_y \\ E_x - iE_y \end{pmatrix} = 0 \quad (4.10)$$

One can see clearly in (4.10) that the two eigenmodes are right-handed circularly polarized waves and left-handed circularly polarized waves. The eigenvalues $\epsilon_{xx} + i\epsilon_{xy}$ and $\epsilon_{xx} - i\epsilon_{xy}$, correspond to the respective refractive indices.

Since linearly polarized light is simply composed of a linear superposition of left and right circular polarizations:

$$\begin{pmatrix} 1 \\ 0 \end{pmatrix} = \frac{1}{2} \begin{pmatrix} 1 \\ i \end{pmatrix} + \frac{1}{2} \begin{pmatrix} 1 \\ -i \end{pmatrix} \quad (4.11)$$

and the reflection coefficients for left- and right-circular light are different, linearly polarized light should undergo a complex rotation. In the polar configuration, the Kerr rotation ($\theta_K = \theta_K^P = \theta_K^S$) of linearly polarized light is:

$$\theta_K = \frac{-2\epsilon_{xy}}{(\epsilon_{xx} + i\epsilon_{xy})(\epsilon_{xx} - i\epsilon_{xy}) - 1} \quad (4.12)$$

4.2.2 Quantum Mechanical Origin

The quantum mechanical origin of Kerr rotation comes from the simultaneous occurrence of exchange splitting and spin-orbit coupling in the band structure of a material. On the microscopic level, the absorption of a photon is governed by electronic energy band structure and Fermi's Golden rule for optical transitions (or, by Kubo's formalism). Kerr rotation is determined by the difference in optical absorption for left- vs. right-circularly polarized light. The relevant terms in this case are the off-diagonal elements of the imaginary part of optical conductivity, which represent the transition between initial state $|i\rangle$ and final state $|f\rangle$ of an electron. This dissipative part of the conductivity tensor can be written in terms of right and left circular momentum operators ($P_{\pm} = P_x \pm iP_y$)[14]:

$$\sigma''_{xy} = \frac{\pi e^2}{4\hbar\omega m^2 V} \sum_{i,f} f_i [1 - f_f] \left[|\langle i | P_- | f \rangle|^2 - |\langle i | P_+ | f \rangle|^2 \right] \delta(E_f - E_i - \hbar\omega) \quad (4.13)$$

where f_i is Fermi-Dirac distribution function indicating the occupation probability of state i , and V is the total volume. The optical conductivity is related to the dielectric constant mentioned previously through:

$$\epsilon(\omega) = 1 + \frac{4\pi i \sigma(\omega)}{\omega} \quad (4.14)$$

Only optical transitions which satisfy energy and momentum conservation are allowed. Energy conservation is assured by the delta function in equation (4.13). Momentum conservation is accounted for by restricting the allowed transition states with the following selection rules:

$$\Delta\ell = \pm 1 \qquad \Delta m_{\ell} = \pm 1 \quad (4.15)$$

The difference in absorption arises from the splitting of majority and minority spin energy levels by the exchange interaction, with energy Δ_{ex} , and the further splitting of degenerate orbitals due to spin-orbit coupling, with energy splitting Δ_{SO} . This is seen schematically in figure 4.2. Spin orbit coupling splits energy levels with different values of m_{ℓ} , and as a consequence right and left circularly polarized have different absorption rates: left circularly polarized light is absorbed in transitions with $\Delta m_{\ell} = +1$ and right circularly polarized light is preferentially absorbed by transitions with $\Delta m_{\ell} = -1$. A sketch of an electric dipole transition from d to p is given in figure 4.2. In this diagram, left and right circular light cause transitions from states with different energy levels ($m_{\ell} = \pm 1$) to the same final state with $m_{\ell} = 0$.

4.3 Time-Resolved MOKE Measurements

The goal of a MOKE measurement is to discern changes in the magnetization of a sample by carefully measuring small changes in the polarization of an incident laser beam. Time resolution is achieved by employing the classic pump probe technique, which entails varying the path length of a pump beam used to excite the sample with respect to the path

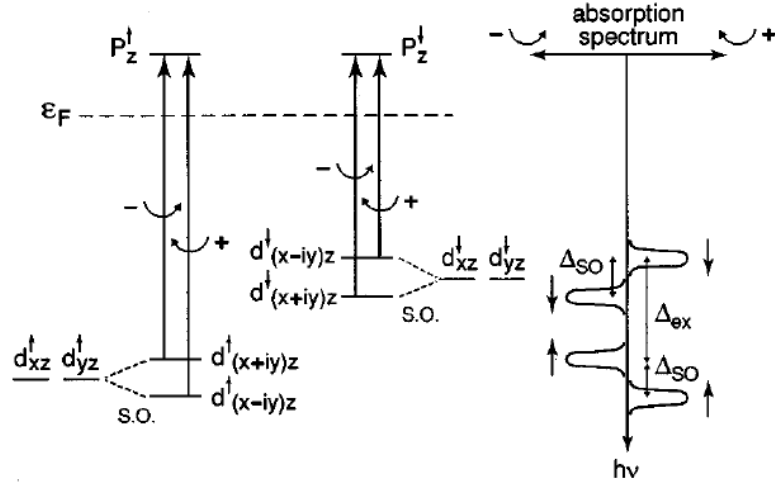


Figure 4.2: Schematic of the energy levels in a ferromagnet, showing the electric dipolar optical transitions for left and right circular light. On the right are the corresponding absorption spectra versus photon energy. Figure from [14]

length of a much weaker probe beam. The changed rotation of the probe beam polarization can then be measured. Note that since it is only the relative arrival time of the two beams that matters, time resolution can be achieved by varying either the path length of the pump or the probe. In the predominant experimental set up used in this thesis, the pump beam approached the sample at near normal incidence, which meant that any change in polarization measured was proportional to change in the z-component of the magnetization. This was not strictly a polar Kerr measurement, however, since the magnetization was not also normal to the sample surface.

Ultrafast optical experiments are made possible by pulsed lasers, which rely on a technique called mode-locking. In this technique a fixed phase relationship is induced between the modes of the laser's resonant cavity. Interference between these modes creates pulsed laser light.

The lower limit of time resolution in an "ultrafast" experiment is set by the pulse width of the laser. The commercial lasers currently available with the shortest pulse width use titanium doped sapphire crystals as the lasing medium, and a pulsed Ti:Sapph oscillator from KM Labs with a pulse width of ~ 80 fs, a wavelength of 800 nm, and a repetition rate of 90 MHz was used for the optical experiments in this thesis. The laser power as it exists the cavity is typically ~ 400 mW in continuous wavelength (cw) mode and ~ 500 mW modelocked, though this can be altered somewhat with fine adjustments of the laser cavity. The Ti:Sapph crystal is pumped with the frequency doubled output of a cw, 532 nm, $Nd:YVO_4$ from Spectra-Physics with an continuous output of 4.5 W.

As in any Kerr experiment, our measurements were done in a reflection geometry. The penetration depth of SRO is 37 nm at a wavelength of 800 nm, and since the majority of films studied in this thesis were < 20 nm thick, the excitation in the samples was essentially uniform. Examination of bare substrates revealed no significant Kerr rotation.

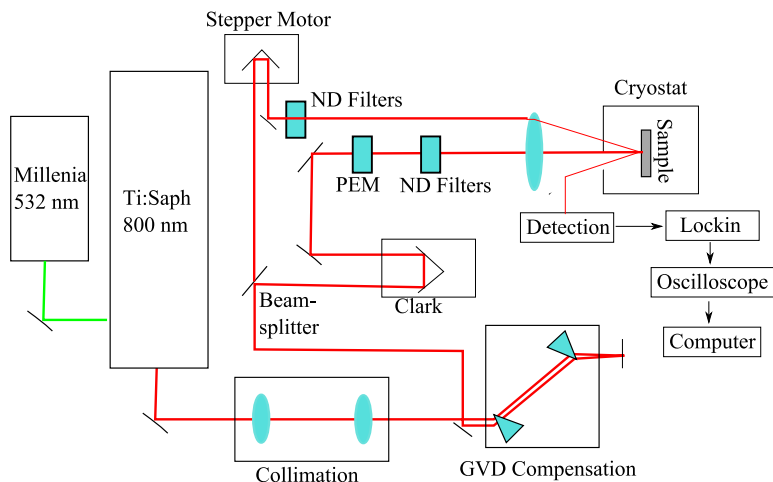


Figure 4.3: Diagram of time-resolved pump-probe setup

4.3.1 Optical Set-up

This section traces the beam path(s) through optical setup, discussing significant components. A diagram of the experimental setup is given in figure 4.3.

When the laser beam emerges from the Ti:Sapph cavity it has a small divergence to it. A pair of identical lenses are used immediately after the laser leaves the cavity to collimate the beam. Identical lens are used to preserve and minimize the beam waist throughout the experiment. The second lens mounted is on a translation stage, which allows the relative position of the lenses to be optimized. To optimize the collimation, use an IR card to view the spot size near the end of the optical setup and make fine adjustments to the position of the second lens with the translation stage.

Once the beam has been collimated, it is sent through a pair of prisms to “chirp” the beam. As the laser beam makes its way through the optics in the setup, various components will increase its temporal width via group velocity dispersion (GVD). This happens because the beam is composed of a small range of wavelengths and the refractive indices of optics are often frequency dependent. To pre-compensate for this effect, a prism pair is used. As light travels through a prism the refractive angle depends on the wavelength of light, so different wavelengths will have path lengths through the prism pair. This allows the frequencies of the beam to be separated and recombined in such a way that negative group velocity dispersion (NGVD) is achieved. This can also be accomplished with a pair of NGVD mirrors. To minimize total GVD in the system, use an auto-correlator near the end of the optical path and adjust the separation between the prisms. To ensure a symmetric path through the prisms, rotate the prisms in the horizontal plane and use an IR card to find the minimum angular deviation of the beam.

After exiting the prism pair, the beam waist is reduced using a lens pair. The front lens has a focal length of 500 mm, and the back lens has a focal length of 100 mm. This is done in anticipation of the size constraint arising from the small head of the Clark

retroreflector.

A 90/10 beam splitter is used to separate the beam into pump and probe beam with 90% of the laser power going to the pump beam. Due to power loss through the optics, by the time the pump beam gets to the sample, the typical pump power is approximately 150 mW. The power of either the pump beam or the probe beam can be changed by neutral-density (ND) filters, which allow the intensity to be adjusted from full power down to <1% of full power. First, let's trace the pump beam.

After the beam splitter the pump beam goes through a pair automated ND filters that allow for remote control of the pump beam intensity. Next it is retroreflected by a Clark fast-scanning delay line. The Clark can be used to continuously vary the path length of the pump beam at a low frequency. (We typically used a frequency of 21 Hz.) The Clark allows for convenient data taking for relatively short time scales (≤ 60 ps) because the frequency of the Clark can be used to trigger the oscilloscope. To align the beam through the Clark, use a mounted razor blade to cut the beam after the retroreflector in half and measure the intensity with a power meter connected to the scope. Then use the knobs on the Clark to adjust the angle of the retroreflector until the signal is relatively flat on the scope. Be sure to check both horizontal and vertical alignment. If you can see the spot moving on an IR card the alignment must be significantly off.

Following the Clark, the pump beam goes through a Hinds photo-elastic modulator (PEM). A PEM works by causing a variable retardation in the phase of light along one of its principle axes. For TRMOKE measurements, the PEM was aligned such that one of the principle axes was along the direction of the incoming polarization of light (horizontal). Note that this is 45° from the physical axes of the PEM head. We used the PEM at $\lambda/2$ retardation in combination with a vertical polarizer (perpendicular to the horizontal laser polarization) to create an intensity modulation of the beam at twice the 50kHz frequency of the PEM. The PEM is also a useful tool for polarization modulation experiments and its instruction manual is an excellent resource.

After the PEM/polarizer combo are a set of mirrors designed to direct the pump beam through the middle of an achromatic doublet lens, such that it will approach a sample in the cryostat at normal incidence. Normal incidence is desirable so that in reflection the pump beam is kept separate from the probe beam. The purpose of the lens is to focus the beam onto a sample to be measured and the 100 mm focal length results in a spot size of less than 100 microns on sample (this was experimentally confirmed in measurements done on patterned SRO into 100 micron strips). At full power, the pump fluence is roughly 0.1 J/cm^2 per pulse.

Turning our attention now to the probe beam: after the beam splitter, the probe beam encounters a large gold retroreflector mounted a Newport motorized translation stage. The motorized stage sits on a long track that allows for up to 500 ps of delay time, useful for measurements done over longer time intervals. Since the position of the Newport stage changes the relative path lengths of the pump and probe beams it is also used to find zero time when initially setting up the optics or after a significant realignment (such as an optic being added or removed). Note that the Newport is frequently referred to as "the Klinger", a popular brand of automated translation stages, in conversation and in data acquisition programs. This retroreflector cannot be adjusted in the same way that

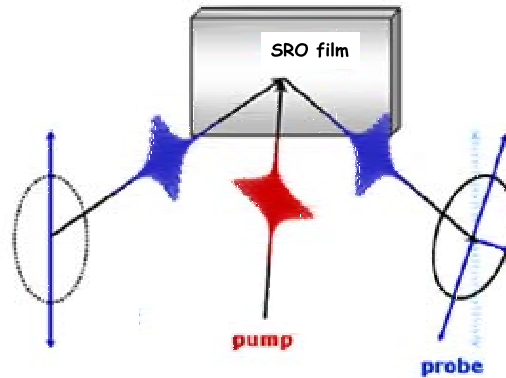


Figure 4.4: Time-Resolved magneto-optical Kerr effect

the Clark retroreflector can be. Instead the probe beam must be aligned by removing the retroreflector from the stage and using a pair of irises to align it, one of which is at the other end of the table. If taking data with the Clark, make sure the Klinger is positioned such that zero time is conveniently located within the path length the Clark moves over.

Past the Klinger are a pair of manually operated ND-filters wheels, a polarizer oriented perpendicular to the polarizer after the PEM in the other beam path, and mirrors designed to send the probe beam off-center through the same achromatic lens mentioned earlier. The pump and probe beam go through the same lens so they will focus at the same spot on a sample, but the probe beam is off-centered so that it will approach the sample at a small angle (around 10°) and reflect from the sample to a pick-off mirror. Note that even though the probe beam approaches at 10° off normal, the index of refraction of SRO (~ 2) means that the angle in the sample is only a few degrees off normal.

The overlap of the pump and probe beam at the focus of the lens is optimized by using a 50 micron pinhole mounted on a 3D translation stage in combination with a power meter. While blocking the probe beam, the position of the pinhole is adjusted until it is at the focus of the pump beam. Then the pump beam is blocked and the probe beam is aligned through the pinhole, using a steering mirror. Note that if the pump and probe beams are at different heights as they approach the achromatic lens, further adjustments to alignment are needed up the beam path. Beams should always be traveling horizontally through the optical setup, except at periscopes.

4.3.2 Detection and Data Acquisition

The Kerr rotation is measured via a balanced detection scheme. After the pick-off mirror the probe beam is sent through an iris, to help block any pump scattering, and a focusing lens, to prevent excessive divergence of the beam after the sample. Next it travels through a motorized half wave plate and a Wollaston crystal which separates the beam into horizontal and vertical components. The purpose of the wave plate is to rotate the polarization of the probe to an angle of 45° so that the intensity of the horizontal and vertical components will be the same after the Wollaston. The two components are then focused

onto the two channels of the Nirvana balanced photodetector. The Nirvana electronically subtracts photocurrent from the two photodiodes, making the detector sensitive to small rotations of the probe beam's polarization, while at the same time reducing noise from laser amplitude fluctuations. Before measurements, the signal output of the Nirvana is carefully minimized by rotating the half-wave plate using a Newport high-precision motorized rotation stage. Note that time-resolved Kerr ellipticity can be measured using the same geometry by balancing the Nirvana DC signal with a quarter wave-plate in place of the half wave-plate.

To measure the Kerr rotation, the linear output of the Nirvana is sent to a Stanford Research Systems SR850 lockin, and referenced at the intensity modulation of the pump beam, i.e. twice the PEM frequency (100kHz). For measurements using the stepper motor, the 100 kHz signal from the lockin is read directly to give the Kerr angle.

For measurements using the Clark, the output from the lockin channel is connected to the input of a Lecroy oscilloscope and triggered with the position output of the Clark. (The frequency and amplitude of the Clark are controlled by a wavefunction generator.) The time trace of the Kerr signal results from averaging this trace on the scope through many cycles of the Clark motion. The position of the Clark is measured as a sinusoidal voltage on the scope, and this is averaged as well. The time-delay of the scan is calibrated by comparing the voltage amplitude of the Clark motion with the physical distance moved by the Clark retroreflector. The distance is measured by finding the difference in step-motor position when the pump-probe $t=0$ time is translated to either end of the the Clark motion. The V/ps ratio is then entered into the data acquisition program.

Note that the most current version of the data acquisition program is designed to account for pump scattering, and will look for the 'C' trace on the scope. The idea is that the probe beam can be blocked, and a pump scattering scan can be taken and then stored in the scope's memory. While the desired scan is taken on trace 'A', the scope can be set up so that 'C' is the active subtraction of the stored scan from the recording data. If this feature is undesirable 'C' can be set to 'A'.

To normalize the size of the measured Kerr angle, the CVI data acquisition program divides the 100 kHz signal from the PEM by the DC signal from the signal channel of the Nirvana, which is measured using auxiliary input one on the SR850. The gain settings on the lockin and differences in gain between the 100 kHz signal and DC signal on the Nirvana are also corrected for by the data acquisition program.

4.3.3 Derivative Measurements

For additional sensitivity, the derivative of $\Delta\Theta_K(t)$ with respect to time can also be measured. This is accomplished by taking advantage of a dual lockin detection scheme. The derivative is measured by setting the amplitude of the Clark motion to less than 500 fs and sending the Nirvana output to a Stanford Research Systems SR830 lockin referenced to the frequency of the Clark. The output of the SR830 is then sent to the input of the 850 lockin, which is referenced to the intensity modulation of the pump beam at 100kHz. Time resolution is achieved by using the Klinger to simultaneously step through the time delay of the probe beam. This is essentially the same configuration as used when taking data with the Clark, only with the second level of averaging coming from a lockin instead

of the scope.

There are a few details to consider when making a derivative measurement. First, the Clark motion cannot be made arbitrarily small, as the motion is no longer sinusoidal below a certain amplitude. The best way to check for this is by looking at the shape of the Clark's motion on the scope as you lower the amplitude. Second the Clark's position output cannot be used as a reference for the first lockin when the Clark amplitude is this small. Instead, use the trigger output of the wavefunction generator used to control the Clark. Also, though the second lockin gain is accounted for by the data acquisition program, the first lockin gain is not and must be recorded manually.

4.3.4 Optical Bleaching Effects

A note of caution regarding ultrafast Kerr measurements: a component of the measured signal is proportional to the change in reflectivity[59]. The dc signal is proportional to the reflectivity as well as the Kerr rotation: $R \Theta_K$. The change in the signal measured in balanced mode is then:

$$d(R \Theta_K) = \Theta_K dR + R d\Theta_K \quad (4.16)$$

The second term is the expected change in Kerr rotation, but the first term is the change in reflectivity multiplied by the dc Kerr signal, which is proportional to the equilibrium magnetization.

Changes in reflectivity typically occur within the first picosecond after excitation, so at longer time scales this effect no longer interferes with the magnetic data. It can obscure fast enough demagnetization times, though.

4.4 Cryostats

The SRO films were cooled in a RC110 Cryo Industries cold-finger cryostat as TR-MOKE measurements were made. For measurements where electrical contact to samples was necessary a Janis ST-300MS cold-finger micro-cryostat was used. In both cryostats, indium foil was used to ensure thermal contact between the cold-finger and the copper sample mount and N-type Apiezon grease was used to mount the samples. The Cryo Industries cryostat was equipped with temperature sensors on the cold-finger and on the sample mount, while the Janis system has only one sensor on the sample mount. Both systems were cooled with liquid He through a transfer line connected to a dewar, which allowed them to consistently reach a minimum temperature of 4.6 K.

Chapter 5

Strain Effects on Anisotropy Orientation and Magnetization Dynamics in SRO

5.0.1 Previous Work: Ferromagnetic Resonance in SRO

Magnetization dynamics of SRO/STO(001) films have been studied previously in our lab[66]. The first observation of ferromagnetic resonance (FMR) in SRO was made, utilizing TRMOKE. FMR had not been seen by conventional methods due to the large magnetocrystalline anisotropy field which predicts a resonance frequency of ~ 200 GHz. The excitation mechanism is as described in section 4.1: thermal excitation causes a sudden rotation of the anisotropy field direction, resulting in the damped precession of the magnetization at the FMR frequency into the new anisotropy field direction. The motion is governed by the LLG equation (see section 3.1.1) and is seen as decaying oscillations by TRMOKE.

Figure 5.1 shows the results of a TRMOKE experiment on a 200nm SRO thin film grown on STO(001). Films of SRO/STO(001) were chosen since they have been best characterized in the literature. Plotted is the Kerr rotation as a function of time after absorption of a pump pulse. Damped oscillations with period on the order of 4 ps become visible below about 80 K, which is approximately one-half of the transition temperature.

The TRMOKE signal offers a wealth of information about the SRO film. The frequency of the FMR oscillations indicates the strength of the anisotropy field. The degree of dampedness of the oscillations reveals the Gilbert damping parameter and offers insight into scattering processes in the sample. The Kerr rotation that persists once the oscillations have damped out provides information about the local excited temperature and how heat diffuses through the sample.

The FMR frequency and the Gilbert damping parameter are conveniently found by taking a Fourier transform into the frequency domain. The center frequency of the Fourier transform is the FMR frequency and the linewidth is proportional to the damping parameter ($\Delta\omega = \alpha\omega/\gamma\mu_0$). Fourier transforms of Kerr measurements taken on a 200nm SRO/STO(001) film in an applied \mathbf{B} field can be seen in figure 5.2. The systematic shift

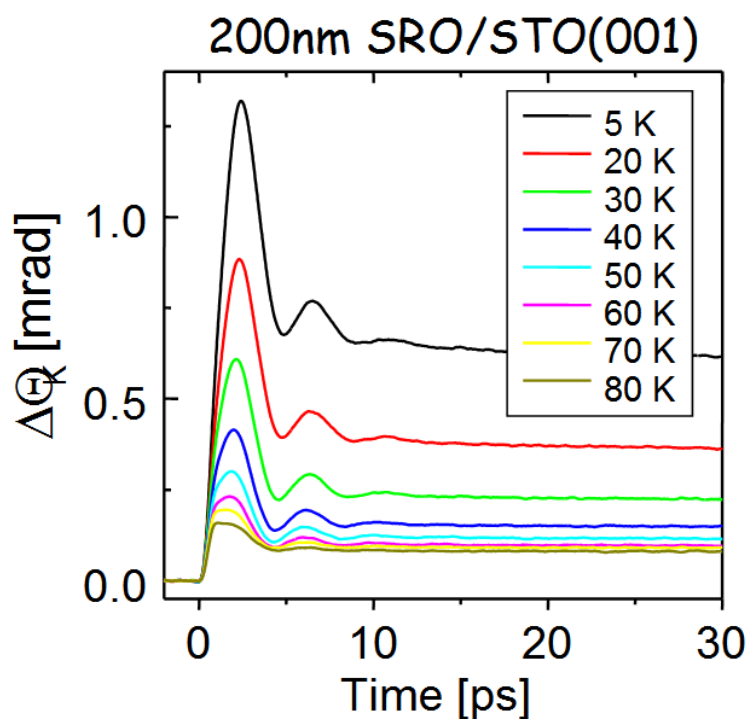


Figure 5.1: Change in Kerr rotation on 200nm SRO/STO(001) as a function of time delay following photoexcitation, in the temperature range $5 < T < 80\text{K}$

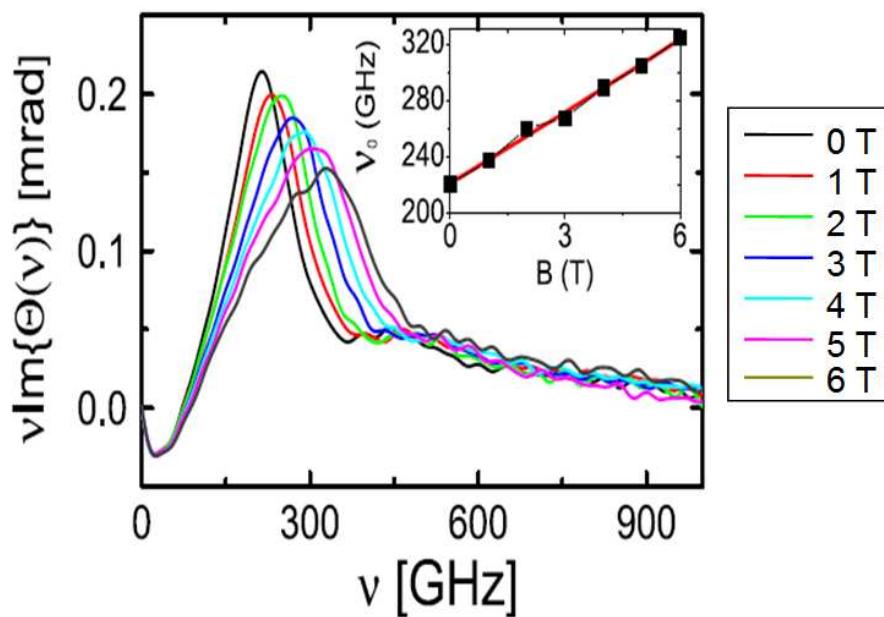


Figure 5.2: Fourier transform of TRMOKE signal in an applied magnetic field of up to 6T

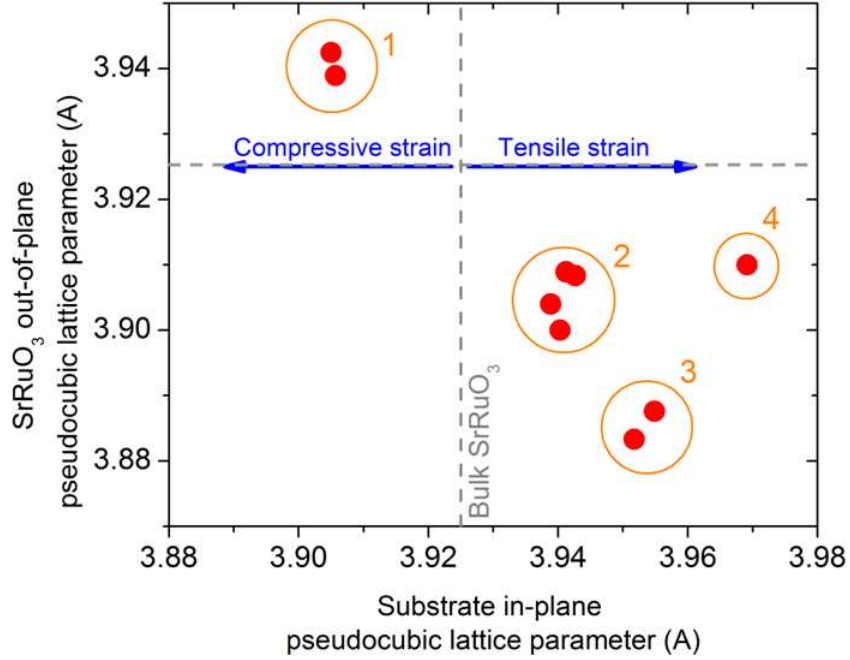


Figure 5.3: Lattice parameters of strained SRO films. The in-plane substrate lattice parameter is plotted on the x-axis and the out-of-plane lattice parameter of the film is plotted on the y-axis.

to higher frequency with increasing B field confirms that the oscillations in figure 5.1 are FMR. The zero field measurement shows a frequency of ~ 220 GHz, consistent with the equilibrium measurement of the anisotropy field in SRO of ~ 7 T.

This previous work measured the TRMOKE signal as a function of temperature, laser intensity, film thickness, and applied magnetic field for SRO/STO(001) films. Now that SRO/STO(001) has been characterized so thoroughly, we are well prepared to detect any changes that might occur due to strain.

5.1 Strained Samples

Thin 10nm films of SRO were grown on STO, GSO, DSO, and $D_{1-\delta}$ SO substrates, all in the (001) orientation. When SRO is grown epitaxially it is forced to match the in-plane lattice parameter of the substrate. In an attempt to preserve the volume of the unit cell, the out plane lattice parameter of the film changes accordingly, (though the volume is not precisely conserved). For instance, for SRO films grown on STO substrates, as the in-plane lattice parameter is compressed, the out-of-plane lattice parameter grows. In figure 5.3, the lattice parameters resulting from growth on STO, GSO, DSO, and $D_{1-\delta}$ SO substrates are shown, as measured by x-ray diffraction. The substrate pseudocubic in-plane lattice parameter is on the x-axis and the pseudocubic in-plane lattice parameter of the film must

be the same. The pseudocubic out-of-plane lattice parameter of the film is plotted on the y-axis. The in-plane and out-of-plane lattice parameters of a single crystal of SRO are indicated by the dashed lines.

Each red dot in figure 5.3 represents a different sample measured. The samples fall into four main categories:

Category one is SRO/STO where there is compressive strain in-plane and the out-of-plane lattice parameter has grown compared to the bulk value for SRO.

Category two is SRO/DSO where the in-plane strain is now tensile and the out of plane lattice parameter has shrunk compared to the bulk.

With category three samples, the trend continues: more tensile strain in-plane, smaller out-of-plane lattice parameter. The substrates in category three are the DSO deficient samples ($D_{1-\delta}$ SO) that were mentioned in section 2.2.2. Note the distinct lattice parameters compared to SRO/DSO.

And the fourth category is SRO/GSO, where the in plane lattice parameter is larger still, but apparently the film has become strained beyond what the SRO crystal structure will bear, and the film has relaxed back toward the bulk out-of-plane parameter. This happens within the first couple of unit cell layers. Had the film not relaxed, the expected out-of-plane lattice parameter would be less than that of the ($D_{1-\delta}$ SO) films.

5.2 Strain Effects on Magnetization Dynamics

The resulting magnetization dynamics on these strained samples, as measured by TRMOKE, can be seen in figure 5.4. Again, the change in Kerr rotation is plotted as a function of time after excitation by a pump pulse at time $t = 0$. The Kerr signals for the various substrates are plotted on the top. In order to more clearly resolve the dynamic behavior, the normalized Kerr signals are plotted on the bottom. Each curve corresponds to a sample with a different set of strain parameters. The corresponding sample is indicated in figure 5.5 by the arrow with coordinating color.

The curve in black is the change in Kerr signal on SRO/STO. It closely resembles the SRO/STO data from section 5.0.1 on a thicker SRO/STO sample. The main difference is that the slope of the change in Kerr rotation is more negative at long times since heat diffuses more quickly from a thinner SRO film.

The curve in dark blue is SRO/DSO, and it looks a bit different. The feature at short times is faster than in SRO/STO, and the oscillation frequency looks like it might be a bit different as well. Also the long lived Kerr rotation (the offset of the TRMOKE signal at ~ 20 ps) is smaller.

The red curve corresponds to SRO/ $D_{1-\delta}$ SO. There is a pronounced difference from SRO/STO in the feature at short times, faster still than was the case on SRO/DSO. But the most striking differences are the relatively large amplitude of the oscillations and the fact that there is almost no change in Kerr rotation at longer times.

The green curve represents another SRO/ $D_{1-\delta}$ SO sample with similar lattice parameters to the previous sample. It is interesting to note, that though the motion is generally

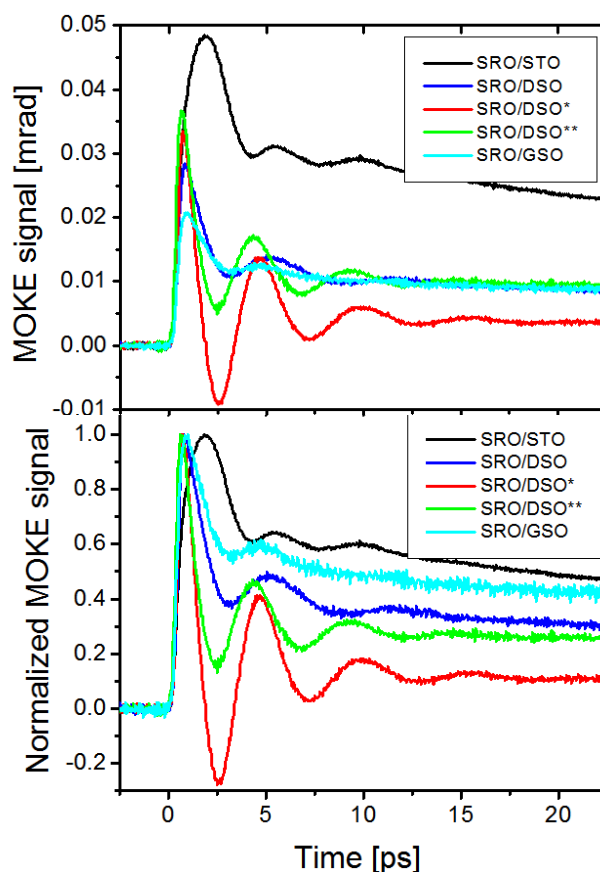


Figure 5.4: TRMOKE signal at 5K after photoexcitation at time $t = 0$ for 10nm SRO films on STO, DSO, DSO*, DSO**, and GSO substrates

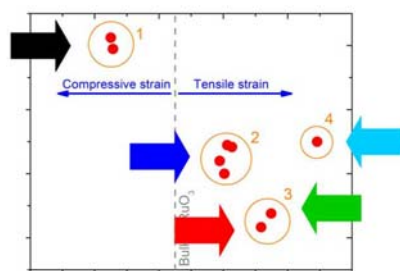


Figure 5.5: Colored arrows indicate the relevant strained samples for the TRMOKE data in the above figure. Compare to figure 5.3

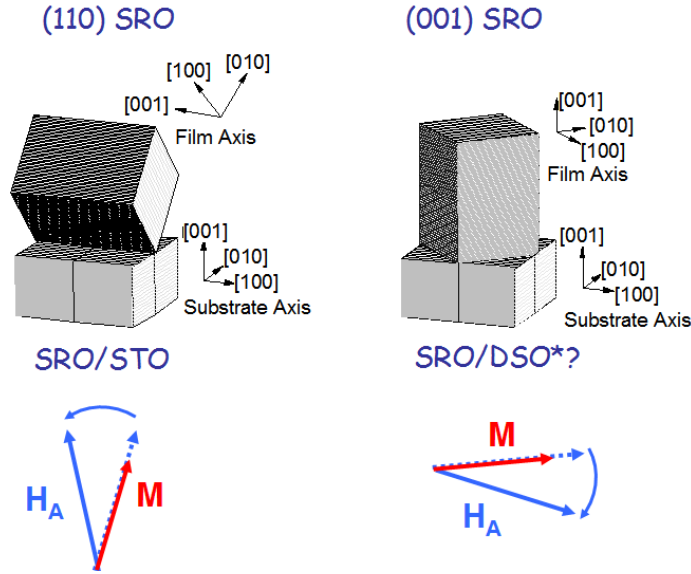


Figure 5.6: Possible orientations of SRO films on (001) oriented substrates. The blue arrows indicate the corresponding motion of the anisotropy field in each case.

very similar, there now there is a distinct offset, even though the lattice parameters have not changed that much. It appears that the magnetization dynamics can be quite sensitive to the lattice parameters. Since the two SRO/D_{1-δ}SO films show different behaviors, the films corresponding to the red and green curves are denoted SRO/DSO* and SRO/DSO**, respectively.

Lastly, the light blue curve is SRO/GSO. This is the case where the film has relaxed back toward the bulk lattice parameters of SRO and the overall amplitude of both the signal and the oscillations is relatively small.

5.3 Analysis: Anisotropy Reorientation as a Function of Strain

Now we would like to try to understand the magnetic behavior that gives rise to the dynamics just seen. It is useful to begin by first examining the two most extreme examples of magnetization dynamics: the black curve corresponding to SRO/STO and the red curve corresponding to SRO/DSO*, seen in figure 5.4.

One of the most noteworthy aspects of the red signal, in comparison to the black signal, is the lack of a measured long lived Kerr rotation. In SRO/STO, the long lived rotation is associated with the changed direction of the anisotropy field due to the localized increase in temperature. But the SRO/DSO* films should be thermally excited to the same degree as the SRO/STO films. This means that, in order to not see any long lived rotation in SRO/DSO*, we must be experimentally insensitive to the change in the magnetocrystalline anisotropy direction. This suggests that the anisotropy field is moving in the plane perpendicular to the \hat{z} direction, since the MOKE signal is only proportional to ΔM_z .

Recall that there are two possible orientations for SRO grown on (001) oriented substrates (see figure 5.6). On STO substrates, SQUID measurements have confirmed that SRO films have (110) orientation with the a- and b-axes both pointing out of the plane at 45°. The anisotropy field is known to rotate as a function of temperature in the a-b plane, so this means that the anisotropy direction moves in a vertical plane.

It should be theoretically possible to grow films of (001) oriented SRO on substrates with (001) orientation. In the (001) orientation of SRO the a- and b-axes would be in the plane and rotated 45 degrees to the substrate axes. In this case we expect the anisotropy field to rotate in a horizontal plane. Unfortunately the paramagnetism of the DSO and GSO substrates prevents accurate SQUID measurements of the SRO films grown on them. While SQUID can't be used to provide an independent confirmation of the easy axis rotation, our data suggests that this is what is happening on the DSO* substrate.

Predictions about the magnetization dynamics can be made based on the orientation of the anisotropy field. Due to the cross product in the first term in the LLG equation (3.10), the initial magnetization motion should be perpendicular to the direction that the anisotropy field moves in. This predicts that for SRO/STO the initial magnetization motion should be perpendicular to the \hat{z} direction, and for SRO/DSO* it should be parallel to the \hat{z} direction. This means that by analyzing the TRMOKE measurements we should be able to extract the film orientation.

In addition to the change in long lived Kerr rotation, there is also a significant difference in the amplitude of oscillation between the two signals. Given a \hat{z} projection of precessional motion at 30° from normal versus in the plane, we expect that the the amplitude of oscillations would be twice as large in the plane, assuming that the motion is circular. But the difference in amplitude exceeds this. We also know from section 3.1.2 that the motion is in general elliptical for small perturbations in the direction of magnetization. Elliptical motion, where the long axis of the ellipse is perpendicular to the a-b plane, could account for the observed dynamics. It is also possible that films with the anisotropy field in the plane are less damped, or that a combination of these two effects is occurring.

5.3.1 Fourier Analysis

To confirm if the predictions regarding magnetization dynamics in the previous section do indeed shed light on SRO film orientation it is helpful to analyze the Fourier transforms of the TRMOKE data.

The Fourier transform is actually taken of the numerical derivative of the TRMOKE signal with respect to time. The reason a derivative is taken first is to help reduce any windowing effects that might occur when calculating the discrete Fourier transform. This is especially relevant when there is still a distinct offset to the TRMOKE signal at the maximum time delay, t_{max} . The computer sums the Fourier transform from $t = 0$ to t_{max} , and interpolates the signal to zero everywhere outside of the measured time window:

$$f(\omega) = \sum_{t=0}^{t_{max}} e^{-i\omega t} f(t) \Delta t \quad (5.1)$$

Since this is the Fourier transform of the derivative, the analyzed function in

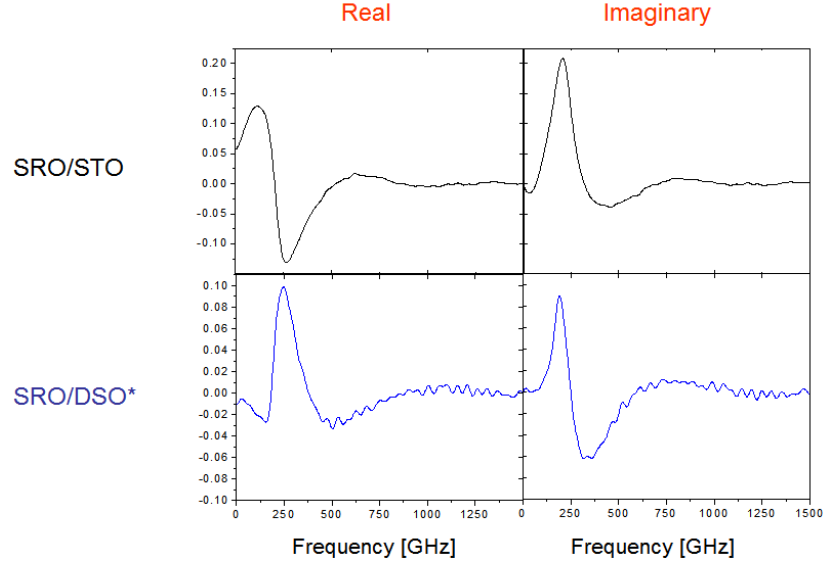


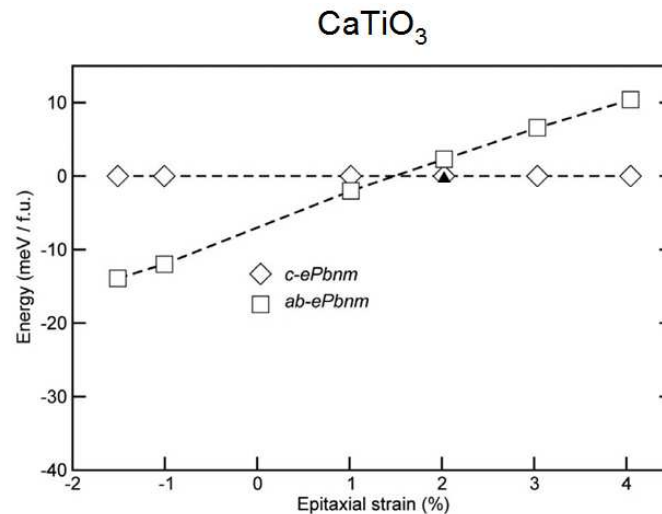
Figure 5.7: Real and imaginary parts of the Fourier transform for SRO/STO (top) and SRO/DSO* (bottom). The signals appear to be out of phase with each other.

frequency space is $i\omega f(\omega)$. For a signal in phase as time $t = 0$, the resonant response is associated with the real part of the Fourier transform, so the relevant quantity would be the imaginary part of the transform after the derivative $Im[i\omega f(\omega)] = \omega Re[f(\omega)]$.

Figure 5.7 shows the real and imaginary parts of the Fourier transform for SRO/STO and SRO/DSO*. The Fourier transforms appear to be close to 90° out of phase with respect to each other. This is what would be expected if the initial motions are perpendicular. So this supports the idea that SRO films grow in the (110) orientation on STO(001) substrates and in the (001) orientation on DSO*(001) substrates.

5.3.2 Theoretical Support

Further support comes from theoretical calculations showing that a change in orientation can be predicted as a function of strain[27]. Figure 5.8 shows a plot of such a predicted switch in orientation for CaTiO_3 . CaTiO_3 has a very similar structure to SRO and the same space group representation, Pbnm. This calculation shows the energy of the orientation with the c-axis out of plane (the (001) orientation) as a function of strain, overlaid with the energy of the orientation where the a and b axes are out of plane (the (110) orientation). For compressive strain the ab-axis out of plane structure is favored, whereas at a certain degree of tensile strain, a crossover to the c axis out of plane structure being energetically favored occurs. This is the same behavior as seen by the TRMOKE experiments on SRO. Though figure 5.8 is of CaTiO_3 , as yet unpublished data by the same group shows the same type of dependence on strain for SRO, through similar calculations.



Eklund, Fennie, Rabe Phys. Rev. B, **79**, 220101

Figure 5.8: Energy of lattice orientation calculated as a function of epitaxial strain for CaTiO₃. From [27].

5.3.3 Support from X-ray Diffraction Experiments

In an effort to experimentally confirm the magnetic orientations, careful XRD measurements were made at the Stanford Nanocharacterization Lab on the SRO/STO and the SRO/DSO* films. The XRD results showed that under compressive stress the pseudocubic perovskite unit cell is tilted and has out-of-plane lattice parameter larger than in-plane. The unit cell of SRO/STO is measured to be monoclinic, with different a and b lattice constants and the angle between them slightly less than 90°. Only one Glazer tilt system satisfies these conditions. Referring to the pseudocubic unit cell, the octahedra must be rotated around c-axis in out-of-phase fashion. The octahedra also have rotations about the a- and b-axes.

Under tensile stress the pseudocubic unit cell is not tilted ($a=b$, roughly). Then the pseudocubic unit cell can end up in two relatively similar configurations but in both cases the unit cell is tetragonal. In both of these configurations the octahedra are not rotated about c-axis, though they still do have rotations about the a- and b-axes.

To summarize these findings: the oxygen octahedra are rotated about the out-of-plane axis under compressive stress and are not rotated around out-of-plane axis under tensile stress. This distinct difference in octahedra symmetry supports the hypothesis that the anisotropy field direction is different in these two samples.

5.4 Intermediate Behavior

Now that we think we have a good understanding of what could be happening in the two most extreme examples of magnetization dynamics, we still need to understand the behavior of the intermediate samples. Since the phase of the Fourier transform proved insightful before, it was examined for all the intermediate samples. The frequency dependent phase is found from the real and imaginary parts of the Fourier transform:

$$\begin{aligned}
 f(\omega) &= \int e^{i\omega t} f(t) dt \\
 f(\omega) &= f_r(\omega) + i f_i(\omega) \\
 \phi(\omega) &= \tan^{-1} \frac{f_i(\omega)}{f_r(\omega)}
 \end{aligned}
 \tag{5.2}$$

Figure 5.9 shows the difference in phase between SRO films grown on various substrates with the SRO/STO sample. The black lines correspond to $\Delta\phi = \pi/2$ and $\Delta\phi = \pi/4$.

At the frequency peak, the phase difference is close to 90° for the two SRO/D_{1- δ} SO samples in category three. Again this is to be expected if the initial motion of the magnetization for these samples is perpendicular to the initial motion of the magnetization for the SRO/STO sample. For the SRO/DSO and SRO/GSO samples in categories two and three the difference in phase is close to 45° .

There appears to be a correspondence between the out-of-plane lattice parameters for these films and the phase difference with SRO/STO. The change in phase vs. out-of-plane lattice parameter is plotted in figure 5.10. The result looks almost linear, indicating a strong correlation between the two.

The question is: “why?”. A first guess might be that there is a mix of c-axis out-of-plane domains and c-axis in-plane domains in these films. If that were true, though, there should be evidence of that in XRD measurements, which instead show that the samples are structurally monodomain.

Another possibility one could imagine is that the anisotropy field deviates from the a-b plane. But the symmetry of SRO is such that the a-b plane is a mirror plane. In other words, there should be no reason for the anisotropy field to deviate away from the a-b plane in one direction vs another.

5.5 Switching Between Orientations

The distinct anisotropy field orientations for SRO films with different degrees of strain raises the question of whether the orientation of a film can be actively changed as a function of applied strain. And if the orientation can be changed for a given film, will the transition between orientations be sudden or continuous? If the symmetry of the initial and final states is the same, the transition must be a sudden, first order transition. But if the degree of symmetry is different in the initial and final states, such as would be the case

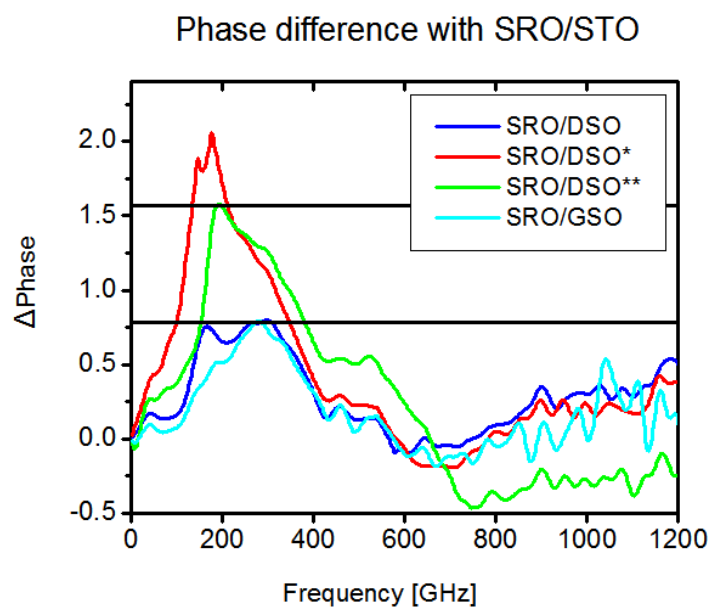


Figure 5.9: Difference in the phase of the Fourier transform for SRO grown on various substrates with SRO/STO. The black lines indicate phase shifts of 45° and 90°

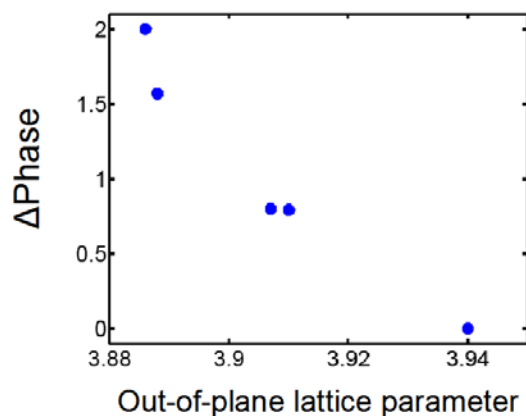


Figure 5.10: Phase difference with SRO/STO at the frequency peak for SRO films from above plot. The near linear dependence suggests a correlation between these two properties.

when transitioning from an orthorhombic structure to a tetragonal structure, it is possible that the transition would be second order and continuous.

Two possible methods of applying strain to an already grown film are through mechanical strain, or by applying an electric field to a piezoelectric substrate. We would have liked to have been able to use either of these methods to test if the anisotropy orientation can be actively changed, particularly the latter, given the potential technological relevance discussed in the introduction of this these. Unfortunately, experimental challenges prevented this from being possible. The essential problem is that a very significant amount of strain is required to change the anisotropy direction. In the interest of guiding future experimentalists who might wish to apply strain to SRO, or use a piezoelectric to apply significant strain to a magnetic sample, some of these experimental challenges are detailed in the next section.

5.5.1 Experimental Challenges

Mechanical strain:

Mechanical strain can be applied to a film by bending it. As a sample is bent, the strain, defined as $\Delta L/L$, is proportional to the thickness of the substrate, and inversely proportional to the radius of curvature, as shown in figure 5.11. (The thickness of the film is negligible compared to the thickness of the substrate.) Depending on whether the sample is bent into a concave or convex shape, the film can be either strained or compressed. The radius of curvature can be found by measuring the divergence of the spot size of a HeNe laser reflected from the surface of the film. The problem with applying mechanical strain is that the sample was found to fracture for strain $\geq \sim 0.07\%$. GaAs has been found to crack under a similar degree of mechanical strain. Since the strain difference between SRO/STO and SRO/DSO* is greater than 1%, this level of strain is insufficient to test if the anisotropy orientation will change as a function of strain.

Strain via piezoelectric:

Attempts to strain SRO by growing it on a piezoelectric focused on using PMN-PT as the piezoelectric substrate. PMN-PT was chosen in part for its relatively close match in lattice parameter to SRO, though its in-plane lattice parameter at $\sim 3.99\text{\AA}$ is even larger than GSO. STO, which has an even smaller in-plane lattice parameter than SRO, has been demonstrated to grow on it[10]. PMN-PT was also chosen for its unusually pronounced piezo-electric behavior. Strain vs. electric field measurements have shown that strains on the order of 1% can be achieved with electric fields of $100\text{V}/10\mu\text{m}$ [91].

Single crystal PMN-PT substrates are commercially available, though not with the level of surface quality necessary for high quality film growth. Mirror-like polishing at the Stanford crystal lab was needed in order to grow SRO with clear XRD peaks. Even with the pre-growth polishing, SRO grown on PMN-PT was of lower quality than SRO grown on the other substrates discussed in this thesis, as measured by XRD and TRMOKE. Clear FMR oscillations were not seen, but there was an observable long-lived Kerr rotation.

Several considerations went into the design of SRO/PMN-PT samples to be studied. The voltage per material thickness required to achieve strains on the order of 1% in

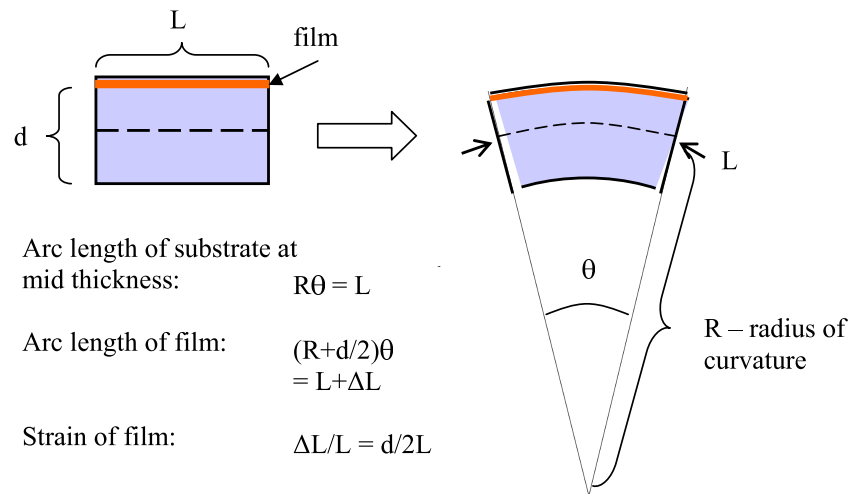


Figure 5.11: Strain induced in a film by bending the substrate.

PMN-PT constrains the electrical contacts to be separated by tens of microns at most. In order to achieve uniform strain in the in-plane lattice parameter, out-of-plane contacts were desirable. In order to satisfy both of these requirements, a scheme was devised where the SRO film would serve as the top contact and the substrate would be thinned from the backside and a metallic contact deposited on it. The plan was to rough polish the entire substrate down to 80-100 microns and then thin portions of the substrate down to 20 microns by ion milling.

Unfortunately PMN-PT substrates are not as robust as STO substrates and it was not possible to rough polish the substrate as thin as we'd hoped. The substrates would frequently fracture in trial runs before 100 micron thickness was reached. This forced us to aim for a rough down to 150 microns, and still the samples were extremely delicate and subject to cracking.

Given the increased thickness of material that needed to be etched post rough polish, and rate at which the ion-milling was expected to remove PMN-PT, we predicted that 50+ hours of ion-milling would be necessary. Unfortunately the ion mill in the Ramesh lab has had problems for quite some time and will only operate for 10 minutes or less, rendering protracted use impossible.

Alternatives to ion-milling were also attempted. An effort was made to chemical etching with HCl, which removed the SRO, and HF, which had no apparent effect on PMN-PT. A Dremmel-like tool was utilized to try to mechanically drill down a small area in the substrate, but shattered the sample above the desired thickness.

An additional problem comes from the heat associated with the large voltages necessary for this project. A change in Kerr rotation is observed when a sinusoidal voltage is applied to SRO and the frequency locked into. Perhaps predictably for a material which is thermally excited, this signal depends on V^2 and is the result of thermal excitation from

the applied voltage. This heating effect is observable for relatively low voltages ($<10\text{V}$). Though the V^2 dependence will eventually saturate at higher voltages, heating should be expected to be a significant noise contribution in such an experiment.

Chapter 6

Magnetization Dynamics Near the Curie Temperature

6.1 Critical Slowing Down

Time resolved MOKE measurements near the Curie temperature have been made previously for films of SRO grown on STO(001) [80, 66]. Increased demagnetization times as the transition temperature is approached from below are observed. The slowing dynamics have been attributed to critical slowing down [80, 49].

The concept of critical slowing down is based on dynamic scaling theory [49, 19]. In the vicinity of a second order phase transition, such as the one that occurs at the Curie temperature of a ferromagnetic, a number of physical properties exhibit scaling behavior. The existence of scaling behavior is dependent on the ability of some physical parameter to be renormalized, e.g., the statistics that govern an individual spin can be applied to a renormalized group of spins, given appropriate adjustments to coupling between spins. When scaling behavior becomes applicable, there are fewer independent variables in a system. In the case of only one independent variable, power law behavior is expected. An example of a parameter that exhibits power law behavior near the Curie temperature is the correlation length.

The correlation length describes the length scale over which a system is ordered. This length scale diverges as a second order transition temperature is approached. The power law that describes this behavior is:

$$\xi = (T_c - T)^{-\nu}. \quad (6.1)$$

where ξ is the correlation length and ν is the critical exponent.

As the correlation length diverges, the time it takes to go from an ordered state to a disordered state diverges as well. This time is called the relaxation time, τ , and is formally related to the correlation length through $\tau = \xi^z$, where z is another critical exponent. Since the demagnetization time was found to scale as a function of the reduced temperature in approximately the same way as the relaxation time, the spin dynamic behavior has been interpreted as critical, though no physical explanation has been offered thus far.

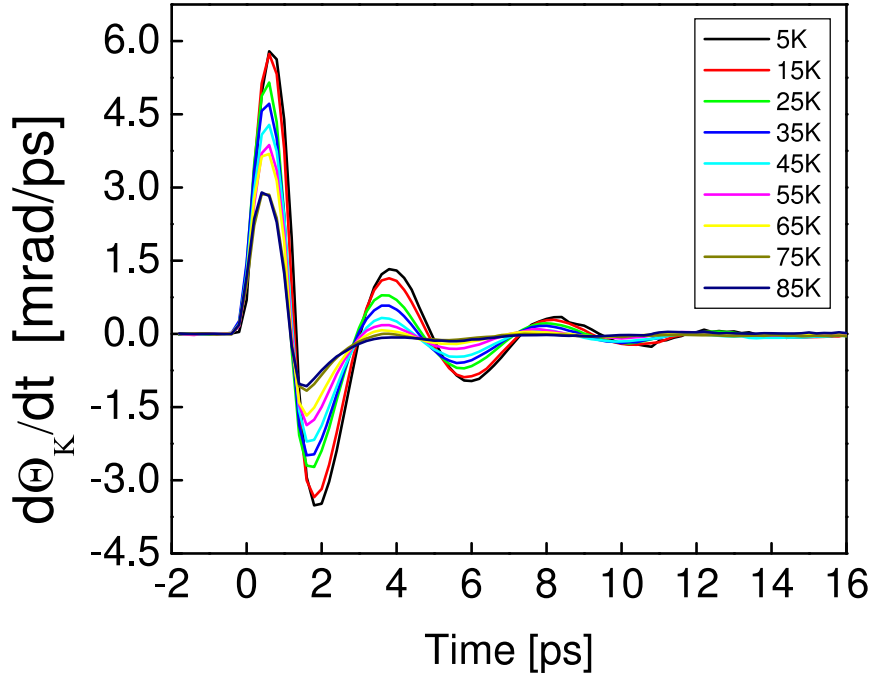


Figure 6.1: Derivative of the change in Kerr rotation as a function of time delay following pulsed photoexcitation, for $5 < T < 85$ K

6.2 Results from Time-Resolved MOKE measurements on SRO/STO(111)

Time-resolved MOKE measurements have been made on thin films of SRO grown on STO(111). For this orientation of STO, SRO grows such that either the orthorhombic [102] or [012] direction is out of the plane. This means that the a-b plane is not vertical, as in the case of (110) SRO previously studied near T_c . Instead, it makes an angle of $\sim 35^\circ$ with vertical. As a result, the Kerr signal is sensitive to a somewhat smaller component of the magnetization.

At low temperature, magnetic oscillations are observed and the sensitivity that derivative measurements of MOKE allow is useful. Figure 6.1 shows the time derivative of $\Delta\Theta_K$ for an 18.5nm SRO/STO(111) sample for the 16ps following excitation by a pump beam, for temperatures between 5 and 85K. Clear ferromagnetic resonance (FMR) oscillations are present, generated by a sudden shift in easy axis direction upon thermal excitation by a pump beam [66]. This motion is described by the Landau-Lifshitz-Gilbert equation with the frequency of oscillation proportional to the strength of the magnetocrystalline anisotropy field, and the damping described by dimensionless phenomenological parameter, α . The motion appears as a decaying oscillation to TRMOKE.

Attempting to model the time derivative of $\Delta\Theta_K$ with a damped cosine reveals that it cannot be fit by such a function for $t < 2$ ps. The feature at short times in figure 6.1

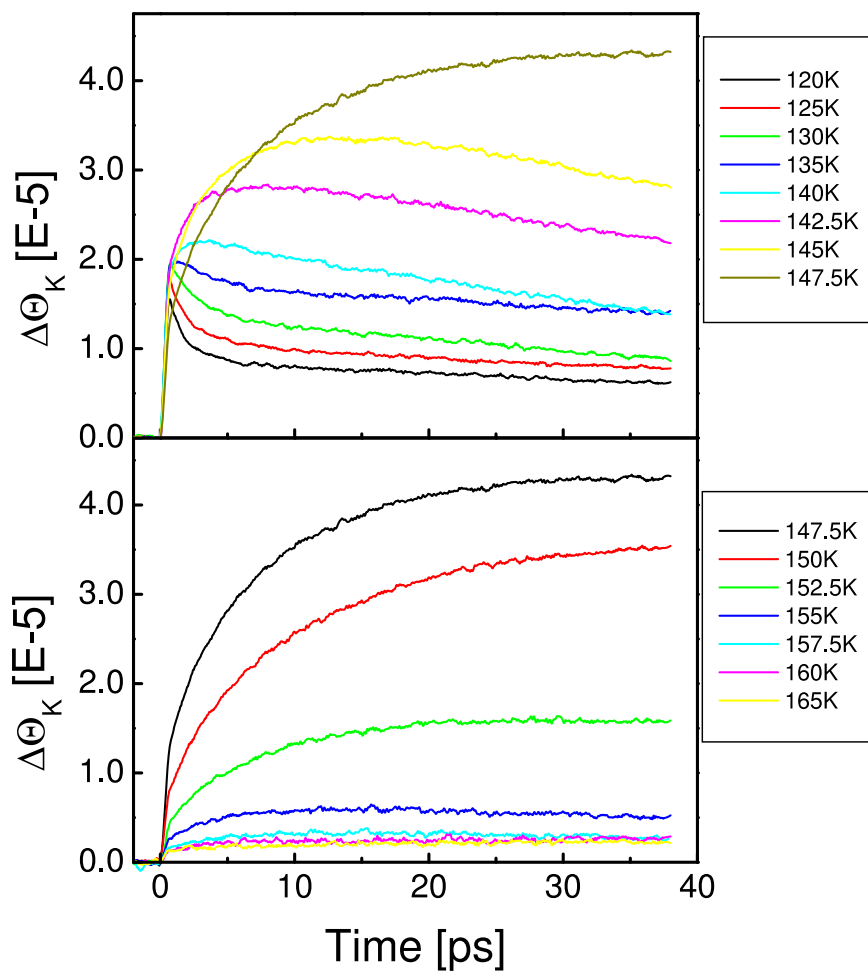


Figure 6.2: Change in Kerr rotation as a function of time delay following pulsed photoexcitation, for $120 < T < 165\text{K}$

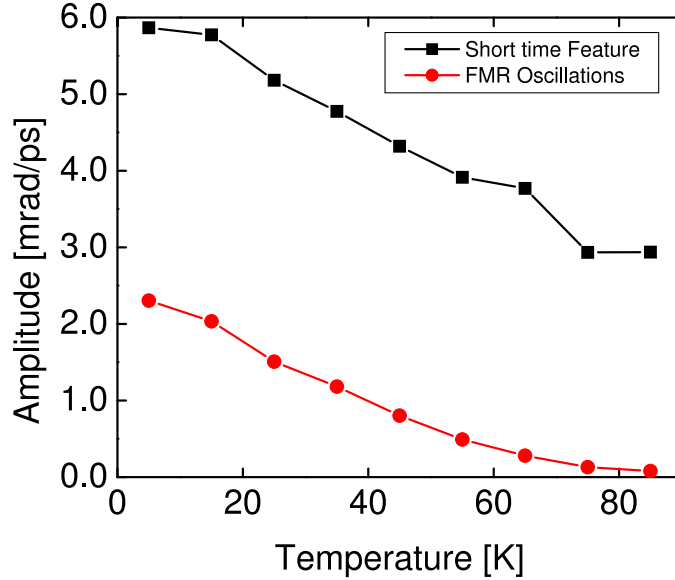


Figure 6.3: Comparing amplitudes of the short time feature and the ferromagnetic resonance oscillations in figure 6.1 as function of temperature.

contains higher frequency components, whereas the oscillations which become clear after 2 ps are at a single frequency. A comparison of the amplitude of the first peak (at $t \sim 0.5$ ps) with the amplitude of the subsequent oscillations (defined as the difference between $d\Delta\Theta_K/dt$ at the peak at ~ 3.5 ps and the dip at ~ 5.5 ps), is shown as a function of temperature in figure 6.3. The constant offset between the two amplitudes indicates that $d\Delta\Theta_K/dt$ is comprised of a superposition of a temperature independent, short-lived component with the longer lived damped oscillations.

Fitting the oscillatory portion of the signal to a damped cosine, the temperature dependencies of the amplitude, frequency, and damping parameter are found, as shown in figure 6.4. Comparing these parameters for SRO/STO(111) to previously published work on SRO/STO(001), seen in figure 6.5, the frequency is found to be somewhat smaller and to change more with temperature. Of particular interest is α , which is also smaller in this orientation of SRO, consistent with the more pronounced FMR oscillations. Strikingly, in both orientations there is a dip in α around 45K, which is relatively stronger in SRO/STO(111).

By taking the time derivative of $\Delta\Theta_K$, the FMR oscillations can be followed until they disappear at elevated temperatures, at which point it becomes simpler to look at $\Delta\Theta_K$ than its time derivative. Figure 6.2 shows $\Delta\Theta_K$ as a function of time for the first 38 ps after excitation by the pump laser, for temperatures between 120K and 165K. The peak in magnitude is the result of the derivative of magnetization with respect to temperature becoming steeper near the transition temperature. A strong temperature dependence of the demagnetization time, τ_M , is seen, with τ_M significantly enhanced near 150K, consistent with previous reports on SRO [80, 66].

$\Delta\Theta_K(t)$ from figure 6.2, normalized by the largest value of $\Delta\Theta_K(t)$ in the first 38

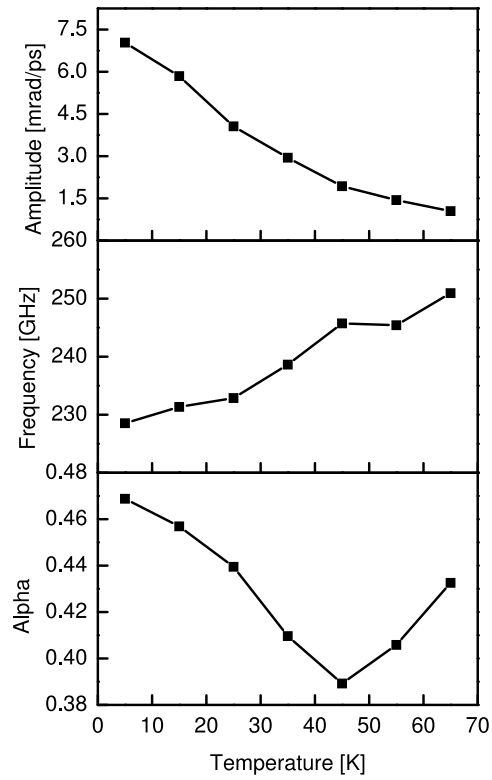


Figure 6.4: Temperature dependence of the (a) amplitude of oscillations, (b) FMR frequency, and, (c) damping parameter for SRO/STO(111)

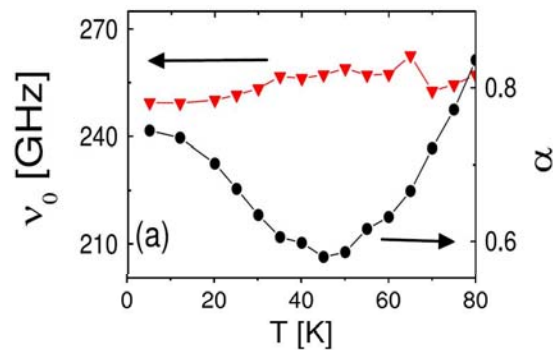


Figure 6.5: Temperature dependence of FMR frequency and damping parameter for SRO/STO(001). Adapted from [66]

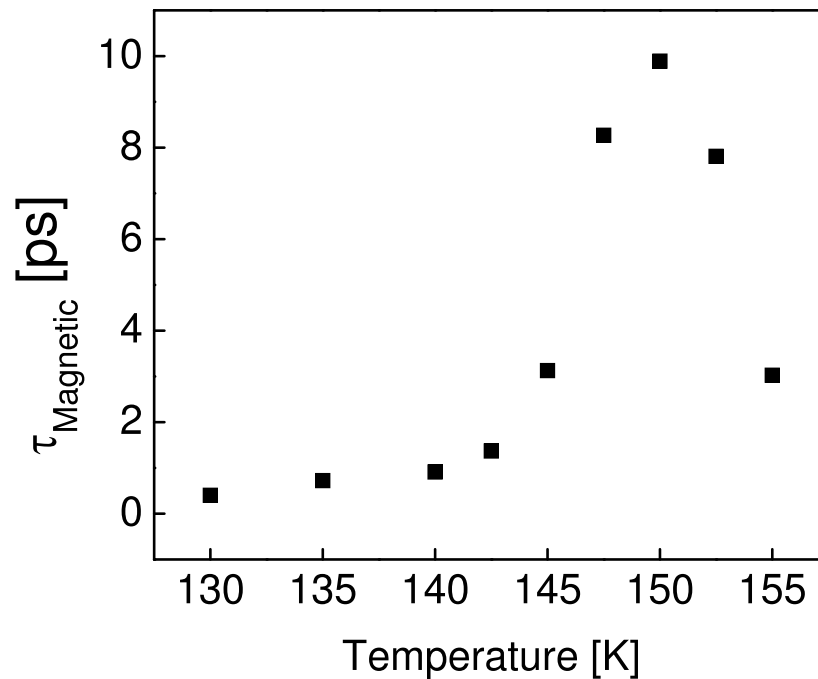


Figure 6.6: The demagnetization time as a function of temperature near T_c

ps, can be fit with the following function:

$$C - Ae^{-t/\tau_M} \quad (6.2)$$

where A is the amplitude of the decay, C is an offset close to one, and the decay time is τ_M . The resulting τ_M , plotted linearly as a function of temperature, is found in figure 6.6. Notably, τ_M increases by more than a factor of 10 over 15K.

6.3 Deriving the Demagnetization time from the Spin-flip time near T_c

As has been alluded to in the introduction and in section 3.3, the related questions of how quickly and by what mechanism a magnetic material can be demagnetized are of great practical and theoretical interest. The notion that spins should take nanoseconds to rotate, with demagnetization resulting from the weak interaction of spins with the lattice, has given way in light of time scales significantly less than 1 ps, and demagnetization is now most frequently attributed to electron-phonon scattering, which can theoretically be responsible for a wide range of demagnetization time scales. It has also been proposed that interband electron-electron scattering at high energies could result in demagnetization, and it should be noted that implicit in this idea is the idea that demagnetization could also result from intraband scattering or interband scattering at low energies.

Efforts to explain demagnetization have been largely phenomenological thus far, understandably, given the daunting challenge of a full microscopic model. In 3TM, the first attempt at modeling ultrafast demagnetization, the dynamics are determined by coupling constants between thermal baths (see 3.3.2). Koopmans' model offers a useful perspective, by following spin in addition to heat (see 3.3.3).

In the following we attempt to understand the behavior of the demagnetization time near T_c with an approach based on Koopmans' model. A general relationship between the laser-induced τ_M and the spin flip time, τ_{sf} , can be derived near the transition temperature based on the concept of detailed balance. Consider a two spin state system. In equilibrium, according to detailed balance, the ratio of the probability of a spin flipping from majority to minority to the probability of flipping from minority to majority should be the Boltzmann factor, $e^{-\Delta_{ex}/kT}$, where Δ_{ex} is the exchange energy gap [75]. The time derivative of the number of majority and minority electrons can then be written:

$$\dot{N}_{maj} = -\dot{N}_{min} = \frac{N_{min}}{\tau_{sf}} - \frac{N_{maj}}{\tau_{sf}} e^{-\Delta_{ex}/k_B T} \quad (6.3)$$

When the sample is thermally excited by a pump beam, the electron temperature is increased by δT_e . The rate of change of spins is then altered in the following way:

$$\dot{N}_{maj} = -\dot{N}_{min} = \frac{N_{min}}{\tau_{sf}} - \frac{N_{maj}}{\tau_{sf}} e^{-\Delta_{ex}/k_B (T + \delta T_e)} \quad (6.4)$$

The demagnetization time should related to the total change in spin, ΔS , from initial to final temperature, where $S = 1/2(N_{maj} - N_{min})/N_{total}$. Assume ΔS , as a function of time, can be written:

$$\Delta S(t) = [S(T_f) - S(T_i)](1 - e^{-t/\tau_M}) \quad (6.5)$$

The demagnetization time, in terms of ΔS and $\dot{S}(0)$, the initial change in the time derivative of the spin, is then:

$$\tau_M = \frac{\Delta S}{\dot{S}(0)} \quad (6.6)$$

The total change in spin can be calculated by taking the derivative of S with respect to T , and multiplying by ΔT_{eq} , the increase in temperature once electrons, phonons, and spins have come into thermal equilibrium with each other:

$$\Delta S = \left. \frac{dS}{dT} \right|_{T=T_0} \Delta T_{eq} = -\frac{1}{4k_B} \left[\frac{\Delta'_{ex}}{T_0} - \frac{\Delta_{ex}}{T_0^2} \right] \Delta T_{eq} \quad (6.7)$$

where we have made the approximation that $\delta T_e \ll T$, and that near the transition temperature, $\Delta_{ex} \ll k_B T$. In the last equation the term proportional to Δ_{ex} is small compared to the term proportional to Δ'_{ex} near T_c .

The initial change in the time derivative of the spin, when the electron temperature has increased, but the spin temperature has not, can be found by taking the derivative with respect to T_e , since the spin temperature, T , has not changed yet.

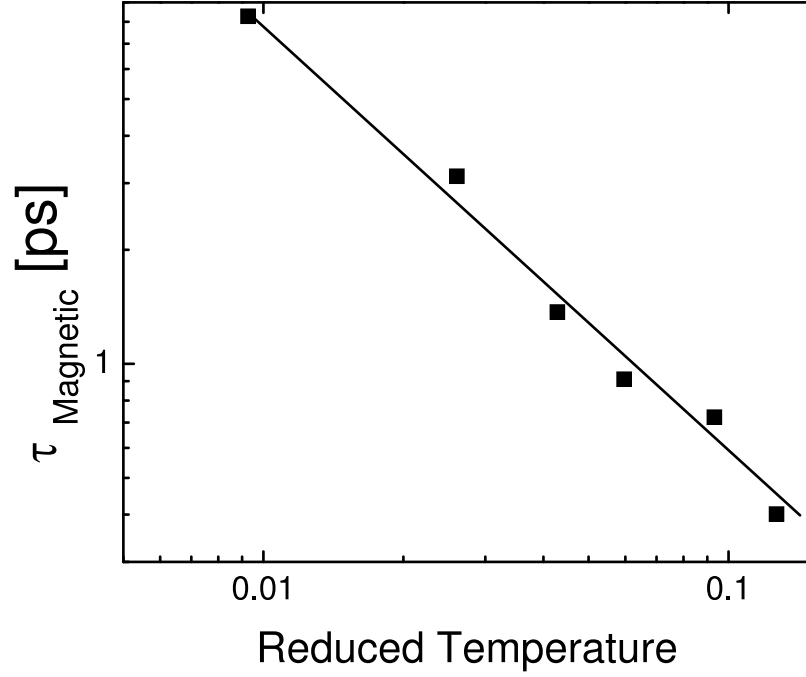


Figure 6.7: Log-log plot of the demagnetization time as a function of reduced temperature near T_c

$$\dot{S}(0) = \left. \frac{d\dot{S}}{dT_e} \right|_{T=T_0} \Delta T_{eq} = \frac{N_{maj}}{N_0 \tau_{sf}} \frac{\Delta_{ex}}{k_B T} \Delta T_{eq} \quad (6.8)$$

Near the Curie temperature $T \sim T_c$, and $N_{maj} \sim N_{min} \sim \frac{1}{2} N_{total}$. Using these approximations and equation (6.6), we find:

$$\tau_M = -\frac{T_c}{2} \tau_{sf} \left(\frac{-\Delta'_{ex}}{\Delta_{ex}} \right) \quad (6.9)$$

where Δ'_{ex} is the derivative of Δ_{ex} with respect to temperature and $\Delta_{ex} \sim (T_c - T)^\beta$, where β is the critical exponent of the order parameter. Taking the derivative, we find $\Delta'_{ex} \sim -\beta(T_c - T)^{\beta-1}$, and thus can write

$$\tau_M = \frac{\beta}{2} \tau_{sf} \left(\frac{T_c}{T_c - T} \right) \quad (6.10)$$

Therefore τ_M scales as $1/(T_c - T)$ near the transition temperature. A fit of 148.8K is found for T_c from the data in figure 6.6. τ_M is plotted log-log as function of reduced temperature, $T_R = (T_c - T)/T_c$ for this fit value of T_c in figure 6.7. The reasonable value of T_c found and the reasonably close fit in figure 6.7 support the validity of equation 6.10.

Note that detailed balance suggests that the demagnetization time scales as $1/T_R$ near the transition temperature regardless of the underlying mechanism of the demagne-

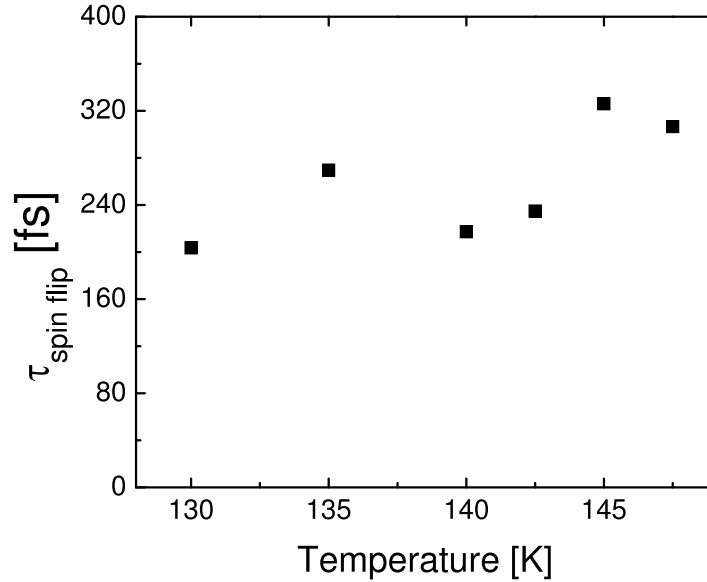


Figure 6.8: Spin flip time at high temperature

tization. Additionally, the critical exponent found is independent of β . It should also be noted that the current situation, where the sample has been excited by a laser, is distinct from critical behavior as typically considered. In general, divergent time scales are linked to divergent length scales, but here excitations of various length scales are not being excited. Instead the length scale is always effectively infinite, having been determined by the laser spot size. τ_{sf} is plotted as a function of temperature for the mean field value of $\beta = 1/2$, which has been shown to be suitable for SRO [47], in figure 6.8. τ_{sf} is revealed to be approximately 200 fs and nearly constant as a function of temperature.

Previous reports of conductivity in SRO give a scattering time of ~ 20 fs near the transition temperature [24]. A comparison of the spin flip time with the scattering time implies a probability of 0.1 that a scattering event results in a spin flip. Though electron-phonon interactions are the most commonly considered source of demagnetization, as mentioned previously, Eliot Yafet-like electron-electron coulomb scattering can also result in demagnetization [64]. This is especially true for materials with strong spin orbit coupling, such as SRO. Additionally in SRO the interaction with the crystal field means that total spin is not conserved[38], so every electron interaction can perturb the spin state.

6.4 Relating the spin-flip time to the damping parameter

Having found a relationship between the demagnetization time and the spin flip time we would like to explore the relationship between these parameters and the damping parameter, α . Intuitively, the damping parameter should be proportional to the spin flip scattering rate, or inversely proportional to the spin flip scattering time: $\alpha \sim 1/\tau_{sf}$. Elliott-Yafet type scattering dissipates energy from motion described by the LLG equa-

tion by disrupting the coherent, collective precession of spins. Spins that have had their angular momentum changed through electron collisions must be pulled back into the precession through the exchange interaction, representing a transfer of energy away from the precessional motion. These collision-mediated spin-orbit coupling effects are thought to be the primary source of Gilbert-type damping in ferromagnets[40]. Again, this should be particularly true in a ferromagnet with strong spin orbit coupling.

Combining the spin flip time and the damping parameter with Planck's constant reveals an energy scale given by:

$$\mathcal{E} \sim \frac{\hbar}{\alpha\tau_{sf}} \quad (6.11)$$

Noting that the values for α and τ_{sf} found in figures 3 and 7, respectively, are approximately constant as a function of temperature, this energy scale for SRO is ~ 7 meV. There are only a few fundamental energy scales applicable to the magnetic system in SRO: the Fermi energy, the orbital splitting energy due to spin orbit coupling, the exchange energy, and the critical temperature, the last two of which are interdependent. The Fermi energy is orders of magnitude larger than 7 meV, and the orbital splitting energy is significantly smaller. The energy associated with the critical temperature, $k_B T_c$, is also of the order of 13 meV. The order of magnitude indicates the relevant energy scale must be the critical temperature. This suggests an underlying connection between the critical temperature (and thus the exchange energy), and damping and spin flip scattering.

Further insight into the relationship between τ_{sf} and α comes from their mutual dependence on avoided crossings in the band structure. In materials with avoided crossings, Elliott-Yafet scattering is enhanced at points in the band structure where the conduction and valence bands are nearly degenerate, and spin-scattering occurs significantly faster[30, 77]. The damping parameter has been shown to depend on avoided crossings theoretically, through its relationship with the zero frequency limit of the dynamic susceptibility[105, 76], and experimentally, through, for example, broadening of the spin-relaxation line width in Al[87].

There is structure in α near 45K, as seen in figure 6.4, potentially linked to avoided crossings. This structure duplicates, and is even more prominent, than structure seen previously in α for a different orientation of SRO[66]. This further strengthens the link between α and the anomalous hall conductivity, speculated in that paper, through near degeneracies in the band structure.

It is also interesting to note that the damping parameter does not depend on the conductivity, which one would expect for an itinerant ferromagnet such as SRO based on the Fermi breathing surface model (see section 3.2.1). Perhaps the relatively high probability of spin flip at a collision overrides the advantage of an increased phase delay between the precessional motion and the distortion of the Fermi surface.

6.5 Demagnetization and damping

Given the relationship found between τ_M and τ_{sf} , and the link between τ_{sf} and α , it should be expected that τ_M is also related to α . And in fact, the initial demagnetization

has been shown to be dominated by avoided crossings in the band structure in Co thin films[87]. Previous work has been done by Koopmans et al to derive a relationship between the demagnetization time and the damping parameter, following the procedure involving Fermi's Golden rule applied to electron-phonon or electron-impurity scattering mentioned previously [57, 23]. At low temperature a simple relationship between τ_M and α was derived:

$$\tau_M = \frac{1}{4} \frac{\hbar}{k_B T_c} \frac{1}{\alpha} \quad (6.12)$$

Applying this equation to SRO at 5K yields $\tau_m \sim 30$ fs, which is unphysical since it is below the total scattering rate of ~ 100 fs at low temperature [24]. Though the specifics of that equation may not apply, a theoretical link between the two is worth pursuing.

Chapter 7

Summary

In this thesis, time resolved optical measurements of magnetization dynamics in SRO thin films have been utilized to explore the effects of epitaxial strain on anisotropy field orientation, and examine the slowing dynamics near the critical temperature. In closing, we highlight a few observations:

The relationship between the electron-orbital hybridization and strain suggests strong dependence of easy-axis rotation on the epitaxial strain on the film. A systematic study of the dynamics in strained SRO films shows a large effect as the strain is tuned from compression to tensile, indicating that at large tensile strains the easy axis is re-oriented in-plane. This result suggests the possibility of switching between magnetic states by applying an electric field to a piezoelectric substrate.

The initial change in magnetization in response to a pump pulse is known to slow significantly as the sample temperature approaches the Curie temperature. Previous explanations have centered on critical behavior as the source of this slowing. This thesis has expanded these results by deriving an equation for the demagnetization time from detailed balanced and finding that the demagnetization time is proportional to the spin flip time and inversely proportional to the reduced temperature. The spin flip time is found to be on the order of a few hundred fs.

We have also found that electron-electron collisions likely play a significant role in demagnetization in SRO, as to be expected for a material with such strong spin orbit coupling.

By relating the momentum-transfer processes in the damping of the ferromagnetic resonance with the spin-flip processes in demagnetization, we find a relationship between the two and the energy associated with the Curie temperature.

Additionally, the study of the damping in SRO/STO(111) shows a feature near 40K, even stronger than that seen in SRO/STO(001), adding additional evidence to the argument that the anomalous Hall effect and magnetization dynamics are related in these films.

Bibliography

- [1] Y Acremann, C H Back, M Buess, O Portmann, A Vaterlaus, D Pescia, and H Melchior. Imaging precessional motion of the magnetization vector. *Science*, 290(5491):492–495, 2000.
- [2] M.B. Agranat, S.I. Ashitkov, A.B. Granovskii, and G.I. Ruckman. Interaction of picosecond laser pulses with the electron, spin and phonon subsystems of nickel. *Sov. Phys/ JETP*, 59(4):804–806, 1984.
- [3] P.B. Allen, H. Berger, O. Chauvet, L. Forro, T. Jarlborg, A. Junod, B. Revaz, and G. Santi. Transport properties, thermodynamic properties, and electronic structure of SrRuO₃. *Physical Review B*, 53(8):4939–4944, 1996.
- [4] Neil W. Ashcroft and N. David Mermin. *Solid State Physics*. Harcourt College Publishers, Fort Worth, Texas, 1976.
- [5] M.N. Baibich, J.M. Broto, A. Fert, F.N. Van Dau, F. Petro, P. Eitenne, G. Creuzet, A. Friederich, and J. Chazelas. Giant magnetoresistance of (001)fe/(001)cr magnetic superlattices. *Physical Review Letters*, 61(21):2472–2475, 1988.
- [6] W. Baltensperger and J.S. Helman. A model that gives rise to effective dry friction in micromagnetics. *Journal of Applied Physics*, 73(10):6516–6518, 1993.
- [7] E. Beaurepaire, J.-C. Merle, A. Daunois, and J.-Y. Bigot. Ultrafast spin dynamics in ferromagnetic nickel. *Physical Review Letters*, 76(22):4250–4253, 1996.
- [8] L. Berger. Side-jump mechanism for the hall effect in ferromagnets. *Physical Review B*, 2(11):4559–4566, 1970.
- [9] G. Bergmann. Analysis of the anomalous hall effect in a double layer of a ferromagnetic and a normal metal. *European Physical Journal B*, 54:19–25, 2006.
- [10] O. Bilani-Zeneli, A.D. Rata, A. Herklotz, O. Mieth, L.M. Eng, L. Schultz, M.D. Biegalski, H.M. Christen, and K. D”orr. SrTiO₃ on piezoelectric PMN-PT(001) for application of variable strain. *Journal of Applied Physics*, 104:054108, 2008.
- [11] G. Binasch, P. Gr”unberg, F. Saurenbach, and W. Zin. Giant magnetoresistance of (001)fe/(001)cr magnetic superlattices. *Physical Review B*, 39(7):4828–4830, 1989.

- [12] J.A.C. Bland and B. Heinrich. *Ultrathin Magnetic Structures I*. Springer-Verlag, Berlin, Germany, 1994.
- [13] W. F. Brown. *Micromagnetics*. Krieger, 1963.
- [14] P. Bruno, Y. Suzuki, and C. Chappert. Magneto-optical kerr effect in a paramagnetic overlayer on a ferromagnetic substrate: A spin-polarized quantum size effect. *Physical Review B*, 53(14):9214–9220, 1996.
- [15] John Rozier Cannon and Felix E. Browder. *The One-Dimensional Heat Equation*. Cambridge University Press, New York, New York, 1984.
- [16] G. Cao, O. Korneta, S. Chikara, L.E. DeLong, and P. Scholttmann. Non-fermi-liquid behavior in single-crystal CaRuO₃: Comparison to ferromagnetic SrRuO₃. *Solid State Communications*, 148:305–309, 2008.
- [17] G Cao, S McCall, M Shepard, J E Crow, and R P Guertin. Thermal, magnetic, and transport properties of single-crystal Sr_{1-x}Ca_xRuO₃ ($0 \leq x \leq 1.0$). *Phys. Rev. B*, 56(1):321–329, 1997.
- [18] G. Cao, W.H. Song, Y.P. Sun, X.N. Lin, and J.E. Crow. Violation of the mott-ioffe-regel limit: High-temperature resistivity of itinerant magnets Sr_{n+1}Ru_nO_{3n+1} and CaRuO₃. *condmat*, 1998. <http://arxiv.org/ftp/cond-mat/papers/0311/0311142.pdf>.
- [19] John Cardy. *Scaling and Renormalization in Statistical Physics*. Cambridge University Press, New York, New York, 1996.
- [20] Sushin Chikazumi. *Physics of Magnetism*. Krieger Publishing Company, Malabar, Florida, 1978.
- [21] M. Cinchetti, M. Sánchez Albaneda, D. Hoffmann, T. Roth, J.P. Wustenberg, M. Krau, O. Andreyev, H.C. Schneider, M. Bauer, and M. Aeschlimann. Spin-flip processes and ultrafast magnetization dynamics in co: Unifying the microscopic and macroscopic view of femtosecond magnetism. *Physical Review Letters*, 97:177201, 2006.
- [22] Bruce M. Clemens, Gary L. Eesley, and Carolyn A. Paddock. Time-resolved thermal transport in compositionally modulated metal films. *Physical Review B*, 37(3):1085–1097, 1988.
- [23] F. Dalla Longa. *PhD thesis: Laser-Induced Magnetization Dynamics*. Eindhoven, 2008.
- [24] J.S. Dodge, C.P. Weber, J. Corson, J. Orenstein, Z. Schlesinger, J.W. Reiner, and M.R. Beasley. Low-frequency crossover of the fractional power-law conductivity in SrRuO₃. *Physical Review Letters*, 85(23):4932–4935, 2000.
- [25] Mary F. Doerner and William D. Nix. Stresses and deformation processes in thin films on substrates. *Critical Reviews in Solid State and Materials Sciences*, 14(3):225–268, 1988.

- [26] C. Ederer and N.A. Spaldin. Weak ferromagnetism and magnetoelectric coupling in bismuth ferrite. *Physical Review B*, 71(6):060401, 2005.
- [27] C.J. Eklund, C.J. Fennie, and K.M. Rabe. Strain-induced ferroelectricity in orthorhombic CaTiO_3 from first principles. *Physical Review B*, 79:220101, 2009.
- [28] R.J. Elliott. Theory of the effect of spin-orbit coupling on magnetic resonance in some semiconductors. *Physical Review*, 96:266–279, 1954.
- [29] V.J. Emery and S.A. Kivelson. Superconductivity in bad metals. *Physical Review Letters*, 74(16):3253–3256, 1995.
- [30] J. Fabian and S. Das Sarma. Spin relaxation of conduction electrons in polyvalent metals: Theory and a realistic calculation. *Physical Review Letters*, 81(25):5624–5627, 1998.
- [31] J. Fabian and S. Das Sarma. Phonon-induced spin relaxation of conduction electrons in aluminum. *Physical Review Letters*, 83(6):1211–1214, 1999.
- [32] L.M. Falicov, Daniel T. Pierce, S.D. Bader, R. Gronsky, Kristl B. Hathaway, Herbert J. Hopster, David N. Lambeth, S.S.P. Parkin, Gary Prinz, Myron Salamon, Ivan K. Schuller, and R.H. Vitora. Surface, interface, and thin-film magnetism. *Journal of Materials Research*, 5(6):1299–1340, 1990.
- [33] Z. Fang, N. Nagaosa, K.S. Takahashi, A. Asamitsu, R. Mathieu, T. Ogasawara, H. Yamada, M. Kawasaki, Y. Tokura, and K. Terakura. The anomalous hall effect and magnetic monopoles in momentum space. *Science*, 302(5642):92–95, 2003.
- [34] K. Fujioka, J. Okamoto, T. Mizokawa, A. Fujimori, I. Hase, M. Abbate, H.J. Lin, C.T. Chen, Y. Takeda, and M. Takano. Electronic structure of SrRuO_3 . *Physical Review B*, 56(11):6380–6383, 1997.
- [35] Q. Gan, R.A. Rao, C.B. Eom, J.L. Garrett, and Mark Lee. Direct measurement of strain effects on magnetic and electrical properties of epitaxial SrRuO_3 thin films. *Applied Physics Letters*, 72(8):978–980, 1997.
- [36] Stephen Gasiorowicz. *Quantum Physics*. John Wiley & Sons, New York, New York, 1996.
- [37] Mathias Getzlaff. *Fundamentals of Magnetism*. Springer-Verlag, Berlin, Germany, 2007.
- [38] J.B. Goodenough. Spin orbit coupling effects in transition metal compounds. *Physical Review*, 171:466–479, 1968.
- [39] Bretislav Heinrich. In J.A.C. Bland and B. Heinrich, editors, *Ultrathin Magnetic Structures II*. Springer-Verlag, Berlin, Germany, 1994.
- [40] B. Heinrich. In J.A.C. Bland and B. Heinrich, editors, *Ultrathin Magnetic Structures III*. Springer-Verlag, Berlin, Germany, 2005.

- [41] B. Heinrich, D. Fraitova, and V. Kambersky. The influence of s-d exchange on relaxation of magnons in metals. *Phys. Stat. Sol.*, 23:501, 1967.
- [42] W K Hiebert, A Stankiewicz, and M R Freeman. Direct observation of magnetic relaxation in a small permalloy disk by time-resolved scanning kerr microscopy. *Phys. Rev. Lett.*, 79(6):1134–1137, 1997.
- [43] J.C. Jiang, W. Tian, X.Q. Pan, Q. Gan, and C.B. Eom. Domain structure of epitaxial SrRuO₃ thin films on miscut (001) SrTiO₃ substrates. *Applied Physics Letters*, 72(23):2963–2965, 1998.
- [44] M.T. Johnson, P.J.H. Bloemen, F.J.A. den Broeder, and J.J. de Vries. Magnetic anisotropy in metallic multilayers. *Reports on Progress in Physics*, 59:1409–1458, 1996.
- [45] V. Kamberský. On the Landau-Lifshitz relaxation in ferromagnetic metals. *Canadian Journal of Physics*, 48:2906–2911, 1970.
- [46] R.J. Kennedy, R. Madden, and P.A. Stampe. Effects of substrate temperature on the growth and properties of SrRuO₃ and CaRuO₃ thin films. *J. Phys. D: Appl. Phys.*, 34:1853, 2001.
- [47] D. Kim, B.L. Zink, F. Hellman, S. McCall, G. Cao, and J.E. Crow. Mean-field behavior with gaussian fluctuations at the ferromagnetic phase transition of SrRuO₃. *Physical Review B*, 67:100406, 2003.
- [48] D. Kirillov, Y. Suzuki, L. Antognazza, K. Char, I. Bozovic, and T.H. Geballe. Phonon anomalies at the magnetic phase transition in SrRuO₃. *Journal of the Society for Industrial and Applied Mathematics*, 51(18):12825–12828, 1995.
- [49] T. Kise, T. Ogasawara, M. Ashida, Y. Tamioka, Y. Tokura, and M. Kuwata-Gonokami. Ultrafast spin dynamics and critical behavior in half-metallic ferromagnet: Sr₂FeMoO₆. *Physical Review Letters*, 85(9):1986–1989, 2000.
- [50] T. Kiyama, K. Yoshimura, K. Kosuge, Y. Ikeda, and Y. Bando. Invar effect of SrRuO₃: Itinerant electron magnetism of Ru 4d electrons. *Physical Review B*, 54(2):R756–R759, 1996.
- [51] L Klein, J S Dodge, C H Ahn, J W Reiner, L Mieville, T H Geballe, M R Beasley, and A Kapitulnik. Transport and magnetization in the badly metallic itinerant ferromagnet SrRuO₃. *J. Phys. Cond.-Matt.*, 8(48):10111–10126, 1996.
- [52] L. Klein, J.S. Dodge, C.H. Ahn, G.J. Snyder, T.H. Geballe, M.R. Beasley, and A. Kapitulnik. Anomalous spin scattering effects in the badly metallic itinerant ferromagnet SrRuO₃. *Physical Review Letters*, 77(13):2774–2777, 1996.
- [53] L. Klein, J.S. Dodge, T. H. Geballe, A. Kapitulnik, A.F. Marshall, L. Antognazza, and K. Char. Perpendicular magnetic anisotropy and strong magneto-optic properties of SrRuO₃ epitaxial films. *Applied Physics Letters*, 66(18):2427–2429, 1995.

- [54] L. Klein, J.S. Dodge, T.H. Geballe, A. Kapitulnik, A.F. Marshall, L. Antognazza, and K. Char. Perpendicular magnetic anisotropy and strong magneto-optic properties of SrRuO₃ epitaxial films. *Applied Physics Letters*, 66(18):2427–2429, 1995.
- [55] L Klein, J R Reiner, T H Geballe, M R Beasley, and A Kapitulnik. Extraordinary hall effect in SrRuO₃. *Phys. Rev. B*, 61(12):R7842–R7845, 2000.
- [56] T. Kobayashi, R. Barker, and A. Yelon. Ferromagnetoelastic resonance in thin films. II. application to nickel. *Physical Review B*, 7(7):3286–3297, 1973.
- [57] B. Koopmans, Ruigrok J.J.M., F. Dalla Longa, and W.J.M. de Jonge. Unifying ultrafast magnetization dynamics. *Physical Review Letters*, 95:267207, 2005.
- [58] B. Koopmans, G. Malinowski, F. Dalla Longa, D. Steiauf, M. F’ahnle, T. Roth, M. Cinchetti, and M. Aeschlimann. Explaining the paradoxical diversity of ultrafast laser-induced demagnetization. *Nature Materials*, 9:259–265, 2009.
- [59] B. Koopmans, M. van Kampen, J. T. Kohlhepp, and W. J. M. de Jonge. Ultrafast magneto-optics in nickel: Magnetism or optics? *Phys. Rev. Lett.*, 85(4):844, 2000.
- [60] Bert Koopmans. In Burkard Hillebrands and Kamel Ounadjela, editors, *Spin Dynamics in Confined Magnetic Structures II*. Springer-Verlag, Berlin, Germany, 2003.
- [61] V. Korenman and R.E. Prange. Damping of spin waves in magnetic metals. *Physical Review B*, 6(7):2769–2777, 1972.
- [62] G. Koster, B.L. Kropman, G.J.H.M. Rijnders, D.H.A. Blank, and H. Rogalla. Quasi-ideal strontium titanate crystal surfaces through formation of strontium hydroxide. *Applied Physics Letters*, 73:2920, 1998.
- [63] P. Kostic, Y. Okada, N.C. Collins, Z. Schlesinger, J.W. Reiner, L. Klein, A. Kapitulnik, T.H. Geballe, and M.R. Beasley. Non-fermi liquid behavior of SrRuO₃: Evidence from infrared conductivity. *Physical Review Letters*, 81(12):2498–2501, 1998.
- [64] M. Krau’s, T. Roth, S. Alebrand, D. Steil, M. Cinchetti, M. Aeschlimann, and H.C. Schneider. Ultrafast demagnetization of ferromagnetic transition metals: The role of the coulomb interaction. *Physical Review B*, 80:180407, 2009.
- [65] M.S. Laad and E. Muller-Hartmann. Origin of the non-fermi liquid behavior of SrRuO₃. *Physical Review Letters*, 87(24):246402, 2001.
- [66] M.C. Langner, C.L.S. Kantner, Y.H. Chu, L.M. Martin, P. Yu, R. Ramesh, and J. Orenstein. Observation of ferromagnetic resonance in SrRuO₃ by the time-resolved magneto-optical kerr effect. *Physical Review Letters*, 102:177601, 2009.
- [67] Laurent-Patrick Lévy. *Magnetism and Superconductivity*. Springer-Verlag, Berlin, Germany, 2000.

- [68] J. Lindner, K. Lenz, E. Kosubek, K. Baberschke, D. Spoddig, R. Meckenstock, J. Pelzl, Z. Frait, and M.L. Mills. Non-gilbert-type damping of the magnetic relaxation in ultrathin ferromagnets: Importance of magnon-magnon scattering. *Physical Review B*, 68:060102, 2003.
- [69] J.M. Longo, P.M. Raccah, and J.B. Goodenough. Magnetic properties of SrRuO_3 and CaRuO_3 . *Journal of Applied Physics*, 39(2):2963–2965, 1968.
- [70] J. M. Luttinger and R Karplus. Hall effect in ferromagnets. *Physical Review*, 94(3):782, 1954.
- [71] Michael P. Marder. *Condensed Matter Physics*. John Wiley & Sons, New York, New York, 2000.
- [72] A F Marshall, L Klein, J S Dodge, C H Ahn, J W Reiner, L Mieville, L Antagonazza, A Kapitulnik, T H Geballe, and M R Beasley. Lorentz transmission electron microscope study of ferromagnetic domain walls in SrRuO_3 : Statics, dynamics, and crystal structure correlation. *J. Appl. Phys.*, 85(8, Part 1):4131–4140, 1999.
- [73] Imada Masatoshi, Atsushi Fujimori, and Yoshinori Tokura. Metal-insulator transitions. *Reviews of Modern Physics*, 70(4):1039–1263, 1998.
- [74] R. Mathieu, A. Asamitsu, H. Yamada, K. S. Takahashi, M. Kawasaki, Z. Fang, N. Nagaosa, and Y. Tokura. Scaling of the anomalous hall effect in $\text{Sr}_{1-x}\text{Ca}_x\text{RuO}_3$. *Phys. Rev. Lett.*, 93(1):016602, 2004.
- [75] N. Metropolis, A.W. Rosenbluth, M.N. Rosenbluth, A.H. Teller, and E. Teller. Equation of state calculations by fast computing machines. *J. Chem. Phys.*, 21:1087–1092, 1953.
- [76] D.L. Mills and S.M. Rezende. *Spin Dynamics in Confined Magnetic Structures II*. Springer-Verlag, Berlin, Germany, 2003.
- [77] P. Monod and F. Beuneu. Conduction-electron spin flip by phonons in metals: Analysis of experimental data. *Physical Review B*, 19(2):911–916, 1979.
- [78] Naoto Nagaosa. Anomalous hall effect - a new perspective. *Journal of the Physical Society of Japan*, 75(4):042001, 2006.
- [79] Theodore C. Oakley. Magneto-optical kerr effect. Technical report, Hinds Instruments, INC, Hillsboro, Oregon, 2005.
- [80] T Ogasawara, K Ohgushi, Y Tomioka, K S Takahashi, H Okamoto, M Kawasaki, and Y Tokura. General features of photoinduced spin dynamics in ferromagnetic and ferrimagnetic compounds. *Physical Review Letters*, 94(8):087202, 2005.
- [81] A. Okazaki and M. Kawaminami. Lattice constant of strontium titanate at low temperatures. *Materials Research Bulletin*, 8:545, 1973.

- [82] N.P. Ong and Wei-Li Lee. Geometry and the anomalous hall effect in ferromagnets. *condmat*, 2005. <http://arxiv.org/abs/cond-mat/0508236v1>.
- [83] M. Onoda, A.S. Mishchenko, and N. Nagaosa. Left-handed ferromagnet. *arXiv:cond-mat/0702379v1*, 2007.
- [84] M Onoda and N Nagaosa. Topological nature of anomalous hall effect in ferromagnets. *J. Phys. Soc. Jap.*, 71(1):19–22, 2002.
- [85] Shigeki Onoda, Naoyuki Sugimoto, and Naoto Nagaosa. Intrinsic versus extrinsic anomalous hall effect in ferromagnets. *Physical Review Letters*, 97:126602, 2006.
- [86] S.S.P. Parkin, C. Kaiser, A. Panchula, P. Rice, B. Hughes, M. Samant, and S.-H. Yang. Giant tunnelling magnetoresistance at room temperature with mgo(100) tunnel barriers. *Nature Materials*, 3(12):862–867, 2004.
- [87] M. Pickel, A. B. Schmidt, F. Giesen, J. Braun, J. Minár, H. Ebert, M. Donath, and M. Weinelt. Spin-orbit hybridization points in the face-centered-cubic cobalt band structure. *Physical Review Letters*, 101:066402, 2006.
- [88] K. Presz and R.W. Munn. Densities of states and anisotropy in tight-binding models. *Journal of Physics C: Solid State Physics*, 19:2499–2507, 1986.
- [89] Z. Qui and S.D. Bader. Surface magneto-optic kerr effect (smoke). *Journal of Magnetism and Magnetic Materials*, 200:664, 1999.
- [90] R. Ramesh and Nicola A. Spaldin. Multiferroics: progress and prospects in thin films. *Nature Materials*, 6:1719–1722, 2007.
- [91] Park S.-E. and T.R. Shrout. Ultrahigh strain and piezoelectric behavior in relaxor based ferroelectric single crystals. *Journal of Applied Physics*, 82:1804, 1997.
- [92] M. Shimizu. Itinerant electron magnetism. *Reports on Progress in Physics*, 44:330–409, 1981.
- [93] K. Shinagawa. In S. Sugano and K. Norimichi, editors, *Magneto-Optics*, volume 128 of *Solid State Sciences*. Springer-Verlag, Berlin, Germany, 2000.
- [94] N.A. Sinitsyn. Semiclassical theories of the anomalous hall effect. *condmat*, 2007. <http://arxiv.org/abs/0712.0183v2>.
- [95] Ralph Skomski. *Simple Models of Magnetism*. Oxford University Press, Oxford, 2008.
- [96] J. Smit. Magnetoresistance of ferromagnetic metals and alloys at low temperatures. *Physica*, 16(6):612–627, 1951.
- [97] J. Smit and H. Beljers. Ferromagnetic resonance absorption in BaFe₁₂O₁₉ a highly anisotropic crystal. *Phil. Res. Rep.*, 10:113, 1955.
- [98] Joachim Stöhr and Hans Christoph Siegmann. *Magnetism: From Fundamentals to Nanoscale Dynamics*. Springer-Verlag, Berlin, Germany, 2006.

- [99] C.-K. Sun, F. Vallée, L. Acioli, E.P. Ippen, and J.G. Fujimoto. Femtosecond investigation of electron thermalization in gold. *Physical Review B*, 48(6):12365–12368, 1993.
- [100] Masuo Suzuki, Kunihiko Kaneko, and Shinji Takesue. Critical slowing down in stochastic processes. *Progress of Theoretical Physics*, 67(6):1756–1775, 1982.
- [101] Guray Tas and Humphrey J. Maris. Electron diffusion in metals studied by picosecond ultrasonics. *Physical Review B*, 49(21):15046–15054, 1994.
- [102] M van Kampen, C Jozsa, J T Kohlhepp, P LeClair, L Lagae, W J M de Jonge, and B Koopmans. All-optical probe of coherent spin waves. *Phys. Rev. Lett.*, 88(22):227201, 2002.
- [103] A. Vaterlaus, T. Beutler, D. Gaurisco, M. Lutz, and F. Meier. Spin-lattice relaxation in ferromagnets studied by time-resolved and spi-polarized photoemission. *Physical Review B*, 46(9):5280–5286, 1992.
- [104] J. Wang, J.B. Neaton, H. Zheng, V. Nagarajan, S.B. Ogale, B. Liu, D. Viehland, V. Vaithyanathan, D.G. Schlom, U.V. Waghmare, N.A. Spaldin, K.M. Rabe, M. Wuttig, and R. Ramesh. Epitaxial BiFeO₃ multiferroic thin film heterostructures. *Science*, 299:22–29, 2003.
- [105] X. Wang, J. R. Yates, I. Souza, and D. Vanderbilt. Ab initio calculation of the anomalous hall conductivity by wannier interpolation. *Phys. Rev. B.*, 74:195118, 2006.
- [106] Chun Yeol You and Sung-Chul Shin. Derivation of simplified analytic formulae for magneto-optical kerr effects. *Applied Physics Letters*, 69(9):1315–1317, 1996.
- [107] J. Zak, E.R. Moog, C. Liu, and S.D. Bader. Universal approach to magneto-optics. *Journal of Magnetism and Magnetic Materials*, 89:107–123, 1990.
- [108] A.T. Zayak, X. X. Huang, J.B. Neaton, and Karin M. Rabe. Structural, electronic, and magnetic properties of SrRuO₃ under epitaxial strain. *Physical Review B*, 74:094104, 2006.
- [109] G.P. Zhang and W. Hubner. Laser-induced ultrafast demagnetization in ferromagnetic metals. *Physical Review Letters*, 85(14):3025–3028, 2000.
- [110] Guoping Zhang, Wolfgang Hubner, Eric Beaurepaire, and Jean-Yves Bigot. In Burkard Hillebrands and Kamel Ounadjela, editors, *Spin Dynamics in Confined Magnetic Structures I*. Springer-Verlag, Berlin, Germany, 2002.